Identification of pharmacological inducers of a reversible hypometabolic state for whole organ preservation

Megan M. Sperry[1,2], Berenice Charrez[1], Haleh Fotowat[1], Erica Gardner[1], Kanoelani Pilobello[1], Zohreh Izadifar[1], Tiffany Lin[1], Abigail Kuelker[1], Sahith Kaki[1], Michael Lewandowski[1], Shanda Lightbown[1], Ramses Martinez[1], Susan Marquez[1], Joel Moore[1], Maria Plaza-Oliver[1,3], Adama M. Sesay[1], Kostyantyn Shcherbina[1], Katherine Sheehan[1], Takako Takeda[1], Daniela Del Campo[1], Kristina Andrijauskaite[4], Exal Cisneros[4], Riley Lopez[4], Isabella Cano[4], Zachary Maxwell[4], Israel Jessop[4], Rafael J. Veraza[4], Leon Bunegin[4], Thomas J. Percival[5], Jaclyn Yracheta[5], Jorge Pena[5], Diandra Wood[5], Zachary Homas[5], Cody Hinshaw[5], Jennifer Cox-Hinshaw[5], Olivia G. Parry[5], Justin J. Sleeter[5], Erik K. Weitzel[5], Michael Levin[1,2,6], Michael Super[1], Richard Novak[1], Donald E. Ingber[1,7,8]*

[1]Wyss Institute for Biologically Inspired Engineering at Harvard University
[2]Department of Biology, Tufts University,
[3]DEVANA group, Faculty of Pharmacy, University of Castilla-La Mancha
[4]Vascular Perfusion Solutions, Inc
[5]RESTOR™, 59th Medical Wing, JBSA, Lackland AFB
[6]Allen Center, Tufts University
[7]Vascular Biology Program & Department of Surgery, Boston Children's Hospital and Harvard Medical School
[8]Harvard John A. Paulson School of Engineering and Applied Sciences
*Corresponding author: Donald E. Ingber, MD, PhD, Wyss Institute at Harvard University, 201 Brookline Ave., Suite 401, Boston, MA, 02215 USA (Em: don.ingber@wyss.harvard.edu)

ABSTRACT

Drugs that induce reversible slowing of metabolic and physiological processes would have great value for organ preservation, especially for organs with high susceptibility to hypoxia-reperfusion injury, such as the heart. Using whole-organism screening of metabolism, mobility, and development in *Xenopus*, we identified an existing drug, SNC80, that rapidly and reversibly slows biochemical and metabolic activities while preserving cell and tissue viability. Although SNC80 was developed as a delta opioid receptor activator, we discovered that its ability to slow metabolism is independent of its opioid modulating activity as a novel SNC80 analog (WB3) with almost 1,000 times less delta opioid receptor binding activity is equally active. Metabolic suppression was also achieved using SNC80 in microfluidic human organs-on-chips, as well as in explanted whole porcine hearts and limbs, demonstrating the cross-species relevance of this approach and potential clinical relevance for surgical transplantation. Pharmacological induction of physiological slowing in combination with organ perfusion transport systems may offer a new therapeutic approach for tissue and organ preservation for transplantation, trauma management, and enhancing patient survival in remote and low-resource locations.

Tissue and organ loss to trauma, disease, and physical injury account for a large proportion of human ailments and approximately $400 billion in annual medical burden.[1] The rapid and reversible slowing of metabolic and other physiological processes, here referred to as 'biostasis', can improve the survival of cells and organs for transplantation. This is currently accomplished clinically by lowering temperature and static cold storage is the standard of care for organ and tissue preservation; however, its long-term use can cause damage to the integrity of the graft.[1–3] Hypothermia also has been used to induce a state of biostasis clinically using *ex-vivo* machine perfusion technologies, for example, during cardiac transplant surgery. Combination of protective agents with perfusion and/or partial freezing approaches have extended preservation times in rat livers and whole pigs,[4,5] and neural modulation approaches

54 have been successful at demonstrating central control of body temperature and general
55 metabolic state.[6,7] However, both mechanical cooling and neural stimulation approaches are
56 challenging to implement in a trauma triage or resource-limited situations, which would be better
57 addressed by pharmaceutical interventions.

58 Several molecular strategies have been proposed to achieve metabolic suppression for
59 organ preservation, including modulating H_2S, AMPK, opioid receptors, microRNAs, HO-1, and
60 Nrf2.[8] H_2S exposure has been reported to induce a hypometabolic state (reduced metabolism
61 and body temperature) in a rodent model, although this was later found to be mediated in part
62 by a low baseline laboratory temperature.[9] The synthetic opioid peptide DADLE also can induce
63 hypometabolism and improve organ preservation via a delta opioid receptor (DOR) mechanism,
64 but with varied results.[10,11] Compounds that directly impact glycolysis and mitochondrial
65 respiration also have been considered for modulating organ metabolism, but many are acutely
66 toxic and not reversible, fail to protect tissues from ischemic injury, or lack drug-like properties.
67 Specifically, reduced functionality of the mitochondrial electron transport chain system without
68 the endogenous antioxidant and anti-inflammatory molecules released by hibernators can result
69 in the release of reactive oxygen species and cause tissue damage.[8]

70 Despite these efforts, there remains a large unmet need for improved tissue and organ
71 preservation approaches across multiple application areas. Thus, in the present study, we set
72 out to identify small molecules that could slow metabolism and mimic states normally induced
73 by hypothermia, hibernation, or torpor, which could be used for preservation of living cells,
74 tissues, and organs *ex vivo*, and potentially *in vivo* as well. Specifically, we required this
75 biostasis approach to be rapidly inducible (< 1 hour) and safely reversible, with major tissue
76 functions returning to control levels within 24 hours.

77 Through survey of the literature, we identified drugs with unintended side effects, such
78 as lowering body temperature, which suggested they might have broad effects on metabolism.
79 During early compound screening, we evaluated known cellular respiration inhibitors (such as

80 rotenone, FCCP, oligomycin A, and Ru360) and torpor inducers from the literature (such as
81 DADLE, JS-K, AMP, sodium sulfide nonahydrate, and BW373u86). Compounds involved in
82 activating the DOR pathway were of particular interest based on prior work suggesting that DOR
83 activation extends the hypothermic preservation time of organs, including the heart.[12] Among
84 these drugs was SNC80, a small molecule drug originally developed as a nonaddictive pain
85 reliever that acts independently of the mu-opioid pathway.[13] This drug caught our attention
86 because it has been shown to induce hypothermia and protect against the effects of spinal cord
87 ischemia in rodents,[13,14] however, further study was required to understand if these observations
88 were related to biostatic effects. To explore whether SNC80 had potential to broadly slow tissue
89 metabolism and physiology, we administered the drug to *Xenopus laevis* embryos and tadpoles,
90 which we and others have previously shown to be useful models for drug screening due to their
91 small size, extrauterine development, and skin permeability to small molecules.[15–18] The
92 *Xenopus* tadpoles were dosed at higher levels than dictated by SNC80's defined IC50 value,
93 with the goal of exploring the effects of SNC80 outside its known pain relief properties and
94 accentuating the drug's "off-target" effects, including hypometabolism.

95 **Demonstration of physiological slowing in *Xenopus***

96 We first assessed SNC80's impacts on mobility, metabolism, and heart activity in
97 *Xenopus*. Behavioral assessment in mobile tadpoles showed that 100 μM SNC80 slows
98 movement relative to vehicle-treated counterparts, reducing activity by approximately 50%
99 within 1 hour, which is rapidly reversible when the drug is removed (**Figure 1a**). SNC80 also
100 suppressed the rate of oxygen consumption to one-third of baseline within 3 hours of treatment
101 (**Figure 1b**) and had extreme suppressive, but fully reversible, effects on heart rate after only 1
102 hour of exposure (**Figure 1c**)**.** Oxygen consumption was reduced in immobile *Xenopus* embryos
103 treated with SNC80 as well (**Figure S1a**), suggesting that its metabolism-suppressing effects
104 are independent of the slowed movement observed in mobile tadpoles.

105 Using *in situ* Matrix-Assisted-Laser Desorption/Ionization-Time of Flight Mass
106 Spectrometry Imaging (MALDI-ToF MSI), we assessed and visualized the biodistribution of
107 SNC80 in the *Xenopus* tadpole. SNC80 was detected within 1 hour of treatment and it appeared
108 in a punctate distribution in the gastrointestinal (GI) tract, gill region and skeletal muscle
109 (**Figures 2a,b**), suggesting full-body delivery of the drug. Specifically, uptake observed in the
110 muscle may be responsible for the slowed motion observed in *Xenopus* activity assays. Past
111 lipidomic studies of hibernating mammals demonstrated the importance of lipid molecules for
112 thermal adaptation during hibernation with significant alterations of lipidomic profiles being
113 observed in liver, plasma, brain, skeletal muscle and cardiac muscle during torpor as compared
114 to the animal's active state.[19,20] Similarly, MALDI-ToF MSI analysis revealed significantly higher
115 levels of acylcarnitine and cholesterol ester in SNC80-treated groups in both skeletal muscle
116 and brain, but not in cardiac tissue (**Figure 2c**). Increased levels of long chain acylcarnitine
117 associated with enhanced mitochondrial fatty acid oxidation are observed during fasting as well
118 as in hibernating brown bears,[21,22] and cholesterol ester levels increase in hibernating ground
119 squirrels.[23] While the increased acylcarnitine and cholesterol ester levels in brain suggest a shift
120 towards beta oxidation of fatty acids, they also have been implicated in other pathways including
121 antioxidant activity and neurotransmission.[24,25]

122 Having confirmed that SNC80 induces slowing of multiple physiological parameters in
123 the whole *Xenopus* organism, we then set out to explore if the molecular basis for these effects
124 is dependent on the DOR pathway. This was important since pre-clinical testing of SNC80 in
125 rodents and non-human primates has demonstrated seizure side effects at higher doses,
126 possibly due to SNC80's direct inhibition of forebrain GABAergic neurons via DOR activity.[26] As
127 SNC80 is a known DOR agonist,[13,14] we next evaluated whether its effects could be mediated
128 by delta opioids. However, when we tested the DOR antagonist, naltrindole (NTI), at double the
129 concentration (200 μM) relative to SNC80 (100 μM), it did not block the hypometabolic effects of

130 SNC80 (**Figure 2d**), suggesting that SNC80 modulates metabolism independent of DOR
131 activation.

132 **Attenuating the delta opioid activity of SNC80**

133 To further test if the physiological slowing effects of SNC80 are independent of DOR
134 activation, we used a medicinal chemistry approach to explore whether we could separate its
135 metabolism slowing and DOR activities. Toward this end, we designed molecular entities void of
136 the distal basic nitrogen (N-ally group within SNC80), which we hypothesized was a critical DOR
137 pharmacophore. This effort led to the development of a novel morpholino compound, WB3
138 (**Figure 3a** & **Supplemental Synthesis Description**), which was synthesized and subsequently
139 tested for DOR binding activity using a radioligand binding assay and non-linear fitting for
140 specific binding to calculate the Hill Slope and IC50 value. A specific binding curve could not be
141 fit for SNC80 due to its high affinity and therefore its IC50 is <4.6 nM, whereas WB3 exhibited
142 an IC50 of 3,470 nM (**Figure 3b**), suggesting almost 1,000 times less DOR binding activity for
143 WB3 compared to SNC80. Subsequently, we screened WB3 in the *Xenopus* swimming, oxygen
144 consumption, and heart rate assays and found that the analog retains physiological slowing
145 properties *in vivo* despite lacking delta opioid activity (**Figure 3c,d,e**). In fact, we observed more
146 potent and rapid effects on swimming with exposure to WB3 compared to SNC80, suggesting
147 that the non-opioid properties of SNC80 may be primarily responsible for its observed
148 physiological effects.

149 **Enhanced preservation of whole pig hearts and limbs perfused *ex vivo***

150 Based on these intriguing findings with *Xenopus* tadpoles, we set out to explore the
151 potential clinical value of SNC80. Cardiac transplant is the gold standard for treating end-stage
152 heart failure; however, it is hindered by donor shortage, limited cardiac graft preservation time,
153 and lack of optimal organ preservation conditions. Currently, hearts are allocated to patients
154 located within 4 hours of organ removal from the donor. Thus, to explore the potential utility of
155 biostasis induction to lengthen the time between organ donation and recipient surgery through

156 pharmacological induction of a hypometabolic state, we perfused surgically explanted whole
157 porcine hearts with SNC80 using a portable, oxygenated perfusion preservation device (VP.S
158 ENCORE®) at subnormothermic temperatures (20-23°C). Prior work has demonstrated that the
159 VP.S ENCORE® enhances cardiac viability over standard of care-static cold storage and hearts
160 perfused in this device for 4 hours demonstrate similar cardiac function to a healthy heart in
161 both preclinical animal models and human deceased donor hearts.[27,28]

162 We investigated the application of a biostasis inducer for preservation of the heart during
163 6 hours of perfusion in the VP.S ENCORE® device. Importantly, with SNC80 treatment, we
164 observed a rapid decline in the heart's oxygen consumption to < 50% of that observed in hearts
165 exposed to the vehicle control, which was sustained over the 6-hour preservation period (**Figure**
166 **4a**). After preservation, hearts were removed from the VP.S ENCORE® and placed in a
167 Langendorff system for reperfusion and evaluation of oxygen consumption and cardiac
168 contractility. This system assesses the left ventricular dP/dT without preload and afterload,
169 thereby allowing the evaluation of the intrinsic contractility of the left ventricle. After 30 minutes
170 of reperfusion and before defibrillation, SNC80-treated hearts had a lower oxygen consumption
171 level than vehicle treated hearts (2.39 ± 1.23 versus 4.28 ± 2.48 ml/min/100g, respectively, at
172 the 30-minute timepoint) (**Figure 4b)** that recovered to normal levels after defibrillation and with
173 increases in temperature (2.49 ± 0.53 and 2.35 ± 0.31 ml/min/100g, respectively, at 60 minutes
174 post-defibrillation) (**Figure 4c**). No evidence of substantial change in left ventricle (LV)
175 contractility or relaxation were detected in SNC80-exposed hearts, either before or after they
176 were defibrillated and exposed to epinephrine (**Figure 4d**).

177 Gene expression analysis of heart biopsy samples showed significant reduction of
178 markers of inflammation (IL-6, IL-8, TNFα), hypoxia (Hif1α), and cell death (TP53, BCL2) in
179 SNC80-treated hearts when compared to vehicle control hearts (**Figure 4e**), and no changes in
180 the mitochondrial ATP synthase marker, ATP5MC3, were observed. Histopathological
181 evaluation showed retention of normal muscle morphology (**Figure 4f**) without signs of tissue

182 edema immediately after perfusion in the VP.S ENCORE®. In some hearts treated with SNC80
183 greater waviness of muscle fibers was observed, possibly indicating a state of muscle
184 contraction.

185 Electrocardiogram (ECG) data revealed that both vehicle and SNC80-treated hearts
186 exhibited irregular beating after perfusion and prior to defibrillation. After defibrillation by electric
187 shock and epinephrine delivery, the P and QRS waveforms were visible in ECGs from 3 of 4
188 SNC80-treated hearts (**Table S1**), indicating that those hearts regained atrial and ventricular
189 depolarization (internal charge of cardiac cells become less negative). The presence of the P
190 and QRS waveforms suggests that the intrinsic atrial and ventricular muscle fiber contractility
191 was preserved and the overall conduction system of the heart was viable. The pulse rates of
192 SNC80-treated hearts were at or near normal range for porcine hearts (70-120 beats/min) after
193 defibrillation. Vehicle-treated hearts exhibited tachycardia following defibrillation, with all
194 exhibiting pulse rates above the normal range for porcine hearts.

195 We also tested organ preservation in porcine limbs, where prolonged ischemia after
196 amputation rapidly decreases the viability of skeletal muscle. Current preservation methods limit
197 the success of limb reimplantation due to complications from rhabdomyolysis, necrosis, and
198 reperfusion injury.[29] Again, we found that the relative metabolic rate measured during 3 hours of
199 SNC80 exposure was significantly lower compared to vehicle-treated limbs (**Figure S2a**).
200 Histopathological evaluation also showed retention of normal muscle morphology with no
201 apparent changes in muscle bundle area (**Figure S2b**) or glycogen content (**Figure S2c**)
202 suggesting that the tissue's potential for ATP synthesis was not compromised after SNC80
203 administration, although an increase in intercellular spacing was observed (**Figure S2d**). We did
204 not observe full recovery of O_2 uptake at the 3-hour time point analyzed in this study (**Figure**
205 **S2c**); however, the porcine limb contains a large amount of fat tissue that may be acting as a
206 depot for the highly lipophilic SNC80, thereby leading to extended stasis under these conditions.

207 **Elucidating potential SNC80 targets and pathways**

208 To gain insight into the molecular basis of SNC80's hypometabolic and other
209 physiological effects, we used thermal proteome profiling (TPP) to assess drug-protein binding
210 and thereby identify previously unknown molecular targets of SNC80 that might be critical for its
211 metabolism slowing activity. TPP of SNC80-treated *Xenopus* tissues revealed 19 direct and
212 indirect binding targets (**Table 1**), including proteins involved in transmembrane transport,
213 mitochondrion activity, and metabolic processes. Two potentially interesting binding targets of
214 SNC80 are the excitatory amino acid transporter 1 (EAAT1; also known as SLC1A3) and the
215 Na^+/Ca^{2+} exchanger 1 (NCX1; also known as SLC8A1), both of which have been identified in
216 cardiac tissue.[30,31] In addition to their individual functions, mitochondrial ATP production has
217 been previously reported to be stimulated through intermolecular interactions between EAATs
218 and NCXs in neurons.[32] If this complex is also present in cardiac tissue, inhibition of EAAT and
219 NCX1 could reduce cellular ATP levels,[33] and thereby play a role in slowing metabolism.
220 Specifically, the blockade of Na^+/Ca^{2+} exchange via interference with EAAT1-NCX1 interactions
221 could prevent the influx of calcium into the mitochondria that is necessary for calcium-sensitive
222 mitochondrial dehydrogenases that fuel ATP synthesis.[34] However, the mitochondrial variant of
223 NCX1 (NCLX) was not included in the *Xenopus* protein library used for TPP analysis so could
224 not be fully evaluated in this study. TPP also identified two additional SNC80-binding proteins
225 located within the mitochondrion: TOMM40 and COX6C. TOMM40 is a translocase located in
226 the outer membrane of the mitochondria that has been implicated in tissue protective effects
227 against late-onset Alzheimer disease[35] and COX6C is the terminal enzyme of the mitochondrial
228 respiratory chain, catalyzing the electron transfer from reduced cytochrome c to oxygen.
229 In addition to interaction with mitochondrial proteins, we detected binding between
230 SNC80 and enzymes involved in other metabolic processes, including alpha-L-fucosidase 2
231 (FUCA2), cysteine conjugate beta-lyase (CCBL1), retinoid isomerohydrolase (RPE65), and
232 acyl-CoA Oxidase 3 (ACOX3). SNC80 also binds to multiple membrane-spanning proteins,
233 including vacuole membrane protein 1 (VMP1) and ABCB1, an ATP-dependent translocase, in

234 addition to NCX1 and EAAT1. The drug also bound to two proteins of the immune system,
235 histocompatibility minor 13 (HM13) and pentraxin 3 (PTX3), as well as two cytoskeletal proteins,
236 calmodulin regulated spectrin associated protein family member 2 (CAMSAP2) and integrin
237 subunit alpha 7 (ITGA7). Interestingly, SNC80 also bound to four ribosomal proteins, RPL4,
238 RPL27A, RPS25, and RRP9, which are frequent targets of antibiotic and antiviral drugs.
239 Collectively, these data suggest that induction of physiological slowing by SNC80 may involve
240 simultaneous modulation of multiple pathways, with critical mechanisms involving mitochondria,
241 membrane-spanning transporters, and possibly other metabolic processes as well.

242 **Stasis induction in cultured human cells and tissues**

243 To explore whether this drug also induces a state of biostasis in cultured human cells,
244 we monitored the effects of SNC80 on oxygen consumption in four different types of cultured
245 human cells ─ human umbilical vein endothelial cells (HUVEC), Caco-2 intestinal epithelial
246 cells, liver sinusoidal endothelial cells (LSEC), and Huh7 liver epithelial cells ─ and analyzed
247 multiple indicators of cellular metabolism using the Seahorse instrument. The latter allows to
248 measure ECAR (extracellular acidification rate), typically serving as proxy for glycolysis activity
249 and oxygen consumption rate (OCR) as a proxy for OXPHOS activity (since mitochondria are
250 responsible for 70%–90% of total oxygen consumption).[36] The Seahorse can also measure
251 other mitochondrial respiration metrics such as ATP production.

252 Treatment with SNC80 (100 μM) suppressed OCR and ATP production relative to
253 control levels within 1.5 hours in epithelial cells derived from intestine and liver (**Figure S3a**)
254 without detectable cytotoxicity (**Figure S4a**), indicating a decrease in cellular metabolism similar
255 to *Xenopus*. Furthermore, we observed a reduction in creatine kinase activity in both epithelial
256 cell types (**Figure S4b**) indicating a decrease in overall cell energy demand.[37]

257 However, cells can also compensate for decreased mitochondrial ATP production by
258 activating other metabolic pathways,[38] indicated by an increase in ECAR. Typically, acidification
259 is linked to lactic acid production due to glycolytic activity. Sometimes however, it can be

260 derived cytosolic reductive carboxylation (CRC) liberating NAD+ (nicotinamide adenine
261 dinucleotide) and H+. We used effluent glutamate levels as an indicator of the metabolic switch
262 to glutamine utilization in CRC ─ a compensation typically used by cells with impaired
263 mitochondrial respiration as a means for NADH recycling.[39]

264 The Caco-2 cells exposed to SNC80 showed a dramatic increase in ECAR and
265 glutamate production (**Figure S4b**), suggesting that the cells activate compensatory
266 mechanisms such as glycolysis and CRC pathway.[40,41] Glutamate generation can account for up
267 to 40% of glutamine utilization in Caco-2,[41] and it is known that glutamine is a very important
268 metabolic fuel and biosynthesis precursor for intestinal epithelium.[42] We can also note that the
269 cancerous origins of Caco-2 give them the ability to rapidly use glycolysis as a source of energy,
270 commonly known as the Warburg effect.[37] Unlike Caco-2, the Huh7 cells showed no change in
271 ECAR nor glutamate (**Figure S4b**) after SNC80 treatment, suggesting that cells did not
272 compensate mitochondrial impairment with increased glycolytic activity or CRC. SNC80 must
273 therefore decrease total ATP production, which was confirmed by detection of a significant drop
274 in the ATP/ADP ratio within liver epithelial cells expressing a fluorescent reporter (**Figure S3b**).

275 When looking at endothelial cells, 2 hours of SNC80 treatment in HUVEC and LSEC
276 reduced mitochondrial ATP production (**Figure S3a**), indicating a decrease in mitochondrial
277 activity and slowing of metabolism. However, it did not alter OCR. We hypothesize that because
278 endothelial cells are highly glycolytic[43] with a low baseline metabolic activity (data not shown),
279 that SNC-80's effect on mitochondrial respiration does not change gut endothelial cell oxygen
280 consumption. HUVEC and LSEC showed no change in ECAR or glutamate (**Figure S4b**),
281 suggesting that the cells are not compensating with additional glycolysis or CRC and that
282 therefore the overall ATP production in the cell line is decreased.

283 Taken together, these results indicate that all four human cell types showed significant
284 decreases in mitochondrial metabolism in response to the biostasis inducer SNC80. However,
285 Caco-2 cells were the only ones that activated compensatory pathways in response to the

286 impaired mitochondrial respiration, while others just allowed for their energy balance to
287 decrease significantly. Our studies also suggested that the metabolism-suppressing effects of
288 SNC80 were most potent in the epithelial cells that were originally derived from highly metabolic
289 tumors.[44]

290 **Metabolic suppression in human Organ Chips**

291 To explore whether this drug also induces a state of biostasis in human cells and tissues, as
292 well as non-cardiac cells, we tested SNC80 in human organ-on-a-chip (Organ Chip) microfluidic
293 culture devices that reconstitute tissue-tissue interfaces and human organ-level physiology with
294 high fidelity *in vitro*.[45] The Organ Chip models reconstitute a tissue-tissue interface between
295 organ-specific epithelium and endothelium across a porous extracellular matrix-coated
296 membrane within a two-channel microfluidic device, and hence allow tissue-tissue cross talk
297 observed *in vivo* that is not normally present in studies with cultured cells, as previously
298 described.[46,47] In this study, we used a Gut Chip lined by Caco-2 intestinal epithelial cells
299 interfaced with HUVECs and a Liver Chip containing Huh7 liver epithelial cells interfaced with
300 LSECs, respectively. However, we modified the Organ Chip design by integrating sensors that
301 allow for live monitoring of oxygen (O_2) and transepithelial electrical resistance (TEER) (tissue
302 barrier function) (**Figure S5a**). Both Organ Chips were treated with SNC80 by flowing the drug
303 in medium for 2 days through the apical and basal channels of the chip, and then removing the
304 drug followed by 7 days of additional culture. We confirmed that the intestinal epithelial cells
305 underwent villus differentiation and accumulated mucus under these culture conditions (**Figure**
306 **S5b**), in addition to maintaining a low oxygen environment after 10-16 days of culture (**Figure**
307 **S5c**) as previously described.[46,47] The Liver Chips also produced albumin and urea at levels (5
308 and 135 µg/day/chip, respectively) (**Figure S5d,e**) that were similar to those measured in Organ
309 Chips lined by primary hepatocytes.[48,49]

310 These studies revealed that SNC80 treatment reduced the respiratory (oxygen
311 utilization) rate in the Gut Chip, resulting in an almost 6-fold increase in extracellular oxygen

levels after 48 hours, which then progressively returned to baseline levels during the 7-day washout period (**Figure 5a**). Similar results were obtained with the more highly metabolic Liver Chip with SNC80 inducing higher levels of extracellular oxygen compared to control chips and this again reversed after drug washout (**Figure 5a**). Importantly, the tissues in both the human Organ Chips remained healthy after 2 days treatment with SNC80 as there was no significant change in barrier function (**Figures 5a,b**), cell growth (**Figure S5g**), or cytotoxicity (**Figures S6c,d**). Similar to the data observed in cell cultures, ATP/ADP ratio in Liver Chips was significantly decreased after 24 and 48h of SNC80 treatment compared to the vehicle control chips. However, ATP/ADP ratio measurements between SNC80 and vehicle control were not significantly different after washout of the drug, indicating that Liver Chip tissues recover their normal metabolic function up to 4 days after treatment (**Figure 5b**).

Collectively, these data suggest that treatment with SNC80 in these physiologically relevant human cells and tissues cultured on-chip in an organ-relevant context resulted in a drop in respiration, with no switch towards glycolysis or reductive carboxylation, since the levels of lactate (**Figure S6e,f**) and glutamate remained unchanged in both chips (**Figure S6g,h**). Thus, in this organ-like microenvironment, the tissues decrease their total ATP production in presence of SNC80, which is accompanied by a global slowing of metabolism.

Discussion

Here we report the discovery that the small molecule drug, SNC80, and its analog WB3, are capable of slowing of multiple physiological processes, and thereby inducing a hypometabolic state without external cooling. Although there is extensive clinical experience using hypothermia to cryopreserve organs during surgery (e.g., cardiac bypass) and for donor transplants, comparatively little work has been done in the area of molecular induction of biostasis without external cooling. We found that SNC80 reversibly suppressed metabolism across multiple cell and tissue types, as well as different species and experimental models, at

338 their basal temperatures, suggesting that this approach could be appropriate for preservation of
339 cells and tissues of the heart, liver, and gut. Critically, integrating this small molecule drug in a
340 commercial organ preservation system with whole explanted pig hearts demonstrated potential
341 for near-term translation and impact of this approach for applications relating to organ
342 preservation and surgical transplantation.

343 Initially developed as a nonaddictive pain reliever, SNC80 was previously shown to
344 induce hypothermia and protect against the effects of spinal cord ischemia in rodents,[13,14] but its
345 broad effects on metabolism were not known. In the present study, treatment with SNC80
346 slowed swimming movement and reduced oxygen consumption rates in a reversible manner in
347 *Xenopus* tadpoles, and it lowered the metabolic rate in non-mobile *Xenopus* embryos as well.
348 Increased levels of acylcarnitine and cholesterol ester in the SNC80-treated *Xenopus* suggested
349 a specific reduction in fatty acid metabolism activity, similar to the metabolic changes observed
350 in hibernating brown bears and ground squirrels.[21–23] Importantly, SNC80 displayed similar
351 metabolism suppressing activities that were reversible in physiologically relevant human Organ
352 Chip microfluidic devices that reconstitute organ-level structures and functions *in vitro*. These
353 experiments also aided in the dose selection for SNC80 (100 μM), which was chosen to
354 maximize suppression of metabolic and activity parameters, while ensuring reversibility of
355 biostasis. These data suggested that induction of a hypometabolic state by this small molecular
356 drug could potentially provide a new paradigm to prolong organ preservation. Indeed, when we
357 perfused explanted porcine hearts and limbs with SNC80, we experimentally confirmed that this
358 biostasis agent can slow metabolism in a whole complex living organs, providing direct support
359 for its potential integration into commercial organ preservation devices that strive to extend the
360 viability of human organs for surgical transplantation.

361 Similar to molecules assessed in the present study, hydrogen sulfide has been shown to
362 induce hypometabolism in whole organs at their basal temperature.[50] Hydrogen sulfide
363 perfusion in porcine kidneys reduced oxygen consumption with similar strength as SNC80

364 across assays, but its activity was less pronounced than WB3. Notably, hydrogen sulfide did not
365 impact ATP levels in porcine kidneys, whereas SNC80 suppressed ATP production in multiple
366 2D cell assays and liver epithelium of the Liver Chip. SNC80 is defined as a highly selective
367 non-peptide DOR agonist drug and other DOR agonists, such as the enkephalin DADLE, have
368 been shown to reduce metabolic demand and protect against oxidative stress, thereby
369 decreasing injury and apoptosis in perfused organs.[8,10,11] Similar to the effect of SNC80 in
370 porcine hearts, DADLE decreased markers of tissue injury and apoptosis in the rat liver.[10]
371 However, DADLE increased ATP levels in liver and increased oxygen consumption in
372 hepatocytes exposed to oxidative stress, suggesting distinct mechanisms compared to SNC80.
373 Prior studies of DADLE found that the DOR pathway was required to alter metabolism
374 and provide protective effects, however, we found that SNC80 suppresses metabolism via a
375 mechanism that is independent of its DOR modulating activity. Instead, we found that SNC80
376 interacts with multiple proteins involved in transmembrane transport, mitochondrion activity, and
377 metabolic processes. Interestingly, one of the identified targets, NCX1, has been previously
378 implicated in control of temperature compensation and autonomous oscillation,[51] suggesting
379 that it plays a key role in the regulation of biochemical reaction speed, cell cycle, and other
380 forms of biological timing, such as circadian rhythm. In addition to its effects on tissues of the
381 nervous system, multiple drugs that target Na^+/Ca^{2+} exchange by NCX, such as the KBR family
382 of drugs, were developed for the treatment of ischemia, reperfusion injury, and heart
383 arrhythmias.[52] In rats, pre-ischemic or post-ischemic treatments with KBR compounds improved
384 recovery of ventricular pump function and reduced reoxygenation-induced injury as measured
385 the reduced release of intracellular components (e.g., lactate dehydrogenase).[52,53] Our results
386 suggest that SNC80 could be acting on the NCX1 transmembrane protein and/or NCX1/EAAT1
387 pathway may result at least in part from induction of a hypometabolic state.[45] Of the tissues
388 impacted by SNC80, the observed effects were most profound on *Xenopus* tadpole heart
389 function and porcine hearts. SNC80 and other opioids have been shown to decrease cardiac

390 inotropy and contractility,[54,55] and prior work has demonstrated that decreases in cardiac
391 inotropy and contractility by opioid agonists may be mediated by opioid receptor-*independent*
392 actions of these drugs.[55] Substantial slowing of heart rate by WB3, which exhibits approximately
393 1,000 times less delta opioid activity than SNC80, further supports this claim. Similar to our
394 findings by TPP, other investigators identified *non-opioid* receptor-mediated actions of these
395 compounds on ion channel function.[55] Changes in contractility were not observed immediately
396 after perfusion with SNC80 in porcine hearts tested here, likely because the SNC80 was
397 washed out of the tissue before contractility was measured; however, future work should
398 continue to monitor these parameters, especially at later time points. Although bradycardia likely
399 contributes to the hypometabolism observed in both systems, we also see reduced metabolic
400 rates in systems lacking cardiac cells, and thus the hypometabolic activity of SNC80 we
401 observed is not completely cardiac-specific.

402 The *Xenopus* and perfused porcine heart systems may be particularly amenable to
403 extreme slowing of cardiac output because these live tissues are surrounded by well-
404 oxygenated medium during treatment, potentially avoiding tissue injury sometimes associated
405 with hypometabolic states. However, the assumption that high oxygen content in the perfusate
406 completely precludes ischemia may not be valid. Assuming adequate flushing during recovery,
407 local vasospasm or a fat micro embolism occurring during perfusion could restrict perfusion flow
408 thereby inducing a localized hypoxic state and HIF1α expression in the tissue. In addition,
409 although HIF1α is primarily known for its role in response to hypoxia, it has some oxygen-
410 independent functions and can be induced by factors other than oxygen levels, such as growth
411 factors and cytokines, which can activate its transcriptional activity even under normoxic
412 conditions. In these cases, HIF1α can regulate genes involved in cell proliferation, metabolism,
413 inflammation, and other cellular processes. Therefore, observation of suppressed HIF1α, as well
414 as the reduction of multiple inflammatory and cell death markers, in the treated porcine cardiac
415 tissue suggests a protective effect of SNC80.

416 Before considering broader applications of SNC80 or any of its analogs, such as whole-
417 body infusion during trauma or infection, it will be critical to consider impacts of this drug not
418 only on the heart but other organ systems as well. In particular, our *Xenopus* data suggest that
419 there could be substantial uptake of SNC80 in the brain, thus potentially impacting tissues of the
420 central nervous system. Therefore, future work should characterize cognitive recovery in
421 organisms receiving systemic delivery of stasis inducers. In addition, whole-body infusion
422 applications may require further pharmaceutical development, including chemical modifications
423 to SNC80 and development of targeted delivery methods to ensure clinical safety.
424 In summary, our findings demonstrate that the small molecule drugs SNC80 and WB3
425 can be used as a biostasis inducer to produce a hypometabolic state, which can provide
426 potential therapeutic value for clinical applications, such as enhanced preservation of organs.
427 The use of a biostatic compound in combination with a self-contained transport system could
428 potentially increase organ viability for sustained times *ex vivo*, thus helping to advance organ
429 and tissue preservation for surgical transplantation.

430 ## Methods

431 ***Xenopus* model.** *Xenopus* embryos were fertilized at Tufts University using procedures
432 reviewed and approved by the Tufts University Institutional Animal Care and Use Committee
433 regulations and transferred to the Wyss Institute. *Xenopus* embryos and tadpoles were housed
434 at 18°C with a 12/12 h light/dark cycle in 0.1X Marc's Modified Ringer's (MMR) medium. All
435 animal experiments and procedures were reviewed and approved by the Harvard Medical
436 School (HMS) Institutional Animal Care and Use Committee regulations.

437 Drugs used in the *Xenopus* studies were dissolved in DMSO to a stock concentration of
438 10 mM and diluted to their final concentrations with a 1% DMSO concentration or less. Media
439 with dosed compound were made fresh and screening was performed in tadpoles at Stages 46-
440 50. The activity of free-swimming tadpoles during and after exposure to drugs were recorded in
441 60 mm dishes using a SONY Alpha a6100 camera with 16 mm objective (Sony Corporation,
442 Tokyo, Japan) against an illuminated background. Mobility was quantified in Matlab (Mathworks,
443 Natick, MA) by mapping differences between frames to a movement index (0 – 1), with 0
444 indicating no movement and 1 indicating maximal movement. Oxygen consumption was
445 measured during *Xenopus* exposure to drugs as a proxy for whole-organism metabolism using
446 the Firesting Optical Oxygen Meter and the Pyro Oxygen Logger software (version 3.317)
447 (Pyroscience GmbH, Aachen, Germany). Oxygen consumption for *Xenopus* embryos was
448 measured using the OxoPlate (PreSens Precision Sensing GmbH, Regensburg, Germany).
449 Oxygen consumption rate for each sample was measured using a linear fit to the oxygen
450 consumption curves in Prism (GraphPad, San Diego, CA). Heart rate was measured by
451 microscopy imaging in *Xenopus* following 1, 2, 4, or 8 hours of drug exposure. Vehicle and
452 drug-treated groups were briefly incubated in 0.01% tricaine (Syndel, Ferndale, WA) to minimize
453 tadpole movement during heart imaging. Videos of heart function were acquired using a ZEISS
454 Axio Zoom.V16 microscope and ZEN BLUE Microscopy software (version 3.1) (Carl Zeiss AG,

455 Oberkochen, Germany) at a rate of 1 frame/100 ms. Heart beats were counted automatically
456 using a custom code in Python. At the completion of experiments, *Xenopus* were euthanized by
457 immersion in 0.2% tricaine for 30 minutes, followed by fixation or bleaching and disposal.
458 **MALDI-ToF.** Tadpoles were embedded in gelatin (0.11 g/mL) and stored in -80C.
459 Embedded tadpoles were sectioned into 16 um-thick slices using a Leica CM1850 (Leica
460 Microsystems, Wetzlar, Germany) onto indium tin oxide (ITO)-coated glass slides (Bruker
461 Daltonics, Billerica, MA) and immediately placed in a vacuum desiccator before matrix
462 application (N=5 tadpoles per condition; N=3 sections/slide). Experiments were duplicated to
463 confirm the reproducibility. The matrix solution was composed of 2,4 Dihydroxybenzoic acid
464 (40mg/mL) in 0.1% formic acid, methanol/water (1:1 v/v) and was made fresh for each
465 application. The HTX-sprayer nebulizer (HTX Technologies, Carrboro, NC, USA) was used to
466 apply the matrix at 80°C at 24 passes over the sample, at a flow rate of 50μL/min, 10 psi
467 pressure and a track speed at 1,250 mm/min. Before imaging, SNC80 spotting with matrix and
468 *Xenopus* lysate was performed to determine the optimal matrix for the best S/N ratio and the
469 least ion suppression from *Xenopus* tissue and to identify which adducts were detectable for
470 each compound for imaging. *In situ* MALDI-ToF imaging was acquired using the rapifleX (Bruker
471 Daltonics, Billerica, MA), in positive ion mode at 1000 Hz in the mass range of 300-990 m/z. The
472 laser raster step spacing was set to 45 μm step size at 500 shots per pixel. External calibration
473 was performed using a red phosphorus slurry drop casted on a region of the ITO slide without
474 tissue. Preliminary processing of the data was performed using FlexAnalysis (Bruker Daltonics,
475 Billerica, MA). Images were normalized by the total ion count and baseline-corrected using Top
476 Hat algorithm with a _baseline width. After MALDI-ToF MSI acquisition, ITO slides were then
477 stained for H&E and imaged using the Cytation 5 (Agilent, Santa Clara, CA) and Epsilon
478 scanner at 3000 dpi to select regions of interest using the open-source program, Qupath.[56]
479 Mass selection windows and signal intensity analysis was conducted with SCiLS Lab (Bruker
480 Daltonics, Billerica, MA), where ions of interest, including SNC80, acylcarnitine and cholesterol

481 ester C18, were chosen with a width of ±0.25 Da. Reference peaks of target analytes were
482 based on previous MALDI-ToF work in *Xenopus* tissues from previous findings,[57] and during
483 spotting of target analytes with MALDI-ToF MS/MS. The mean signal intensity of the defined
484 regions of interest were obtained with each ion of interest.

485 **Radioligand binding assay.** To assess binding of WB3 to the delta opioid receptor, we
486 tested WB3 and SNC80 at 8-concentrations with 3-fold serial dilutions starting at 10 μM
487 (Reaction Biology, Malvern, PA). Binding of the tracer [3H]-DADLE (10 nM) was assessed in the
488 presence of each concentration of WB3 and SNC80 and the [3]-DADLE signal was fit to a dose-
489 response curve to quantify the Hill Slope and IC50 values.

490 **Thermal proteome profiling.** To identify drug-bound targets based on altered thermal
491 stability, *Xenopus* tadpoles were treated with either SNC80 or vehicle for 2 hours. *Xenopus*
492 were euthanized in 20X tricaine and then transferred back to their respective drug solutions to
493 ensure drug effect is not lost during heat treatment. *Xenopus* samples were incubated at 9
494 temperature points (30C, 35C, 40C, 44C, 48C, 52C, 56C, 60C, 65C) using a PCR machine (3
495 minutes heat time per condition, 3 tadpoles per condition) for both drug treated and vehicle
496 treated groups. After transfer to room temperature, liquid was aspirated from samples and
497 samples were snap frozen in liquid nitrogen. Samples were lysed in 100 μl of PBS + 0.4 % NP-
498 40 with 4 cycles of freeze/thaw. 11μl of each of the 9 temperatures were pooled in one tube and
499 samples were centrifuged at 13,000 RPM for 75 minutes, at 4C. Proteins were reduced and
500 alkylated with 10 mM DTT and 15 mM IAA for 15 minutes at 65C and 30 minutes at room
501 temperature, respectively. Proteins were then precipitated with 8 volumes of ice-cold acetone
502 and 1 volume of ice-cold methanol overnight. Digestion was carried for 4 hours in 50 mM Tris ph
503 8 + 0.75 mM Urea + 1μg trypsin/LysC at 37 Celcius with agitation. Another 1 μg of trypsin/LysC
504 was added and digestion was continued overnight. Peptides were purified by reversed phase
505 SPE and analyzed by LC-MS/MS (PhenoSwitch Bioscience, Sherbrooke, QC, Canada). LC-
506 MS/MS acquisition was performed with a ABSciex TripleTOF 6600 (ABSciex, Foster City, CA,

507 USA) equipped with an electrospray interface with a 25 µm iD capillary and coupled to an
508 Eksigent µUHPLC (Eksigent, Redwood City, CA, USA). Analyst TF 1.8 software was used to
509 control the instrument and for data processing and acquisition. Samples were acquired twice in
510 SWATH acquisition mode using gas phase fractionation. The source voltage was set to 5.5 kV
511 and maintained at 325C, curtain gas was set at 45 psi, gas one at 25 psi and gas two at 25 psi.
512 Separation was performed on a reversed phase Kinetex XB column 0.3 µm i.d., 2.6 µm
513 particles, 150mm long (Phenomenex) which was maintained at 60C. Samples were injected by
514 loop overfilling into a 5µL loop. For the 60 minutes LC gradient, the mobile phase consisted of
515 the following solvent A (0.2% v/v formic acid and 3% DMSO v/v in water) and solvent B (0.2%
516 v/v formic acid and 3% DMSO in EtOH) at a flow rate of 3 µL/min. GPF files for both acquisitions
517 were analyzed on a previously generated 3D ion library. Each GPF file was analyzed using 10
518 peptides per protein, 4 MS/MS transition per peptide, 12.5-minute RT window and 25 ppm XIC
519 width in Peakview (Sciex). The reported quantification for a protein is the sum of all the correctly
520 integrated peptides (FDR<0.05) in both GPF files.

521 **Human Cell Cultures:** Caco2 intestinal epithelial cells were grown in high glucose
522 (4.5g/L) DMEM (Gibco), 10% FBS (Gibco) and 1% penicillin/ streptomycin (Gibco) and
523 subcultured every 2-3 days at 1:6 ratio. For all experiments, cells were used between passage
524 59 and 64. HUVE cells were maintained in EBM-2 (Lonza) media with EGM-2 BulletKit (Lonza),
525 2% FBS and 1% penicillin/streptomycin (Gibco) and subcultured every 2-3 days at 1:6 ratio. For
526 all experiments, cells were used between passage 3 and 7. HuH-7 liver epithelial cells were
527 maintained in DMEM with 4.5g/L glucose (HyClone), 10% FBS and 1% penicillin/ streptomycin
528 (Gibco). We also obtained wild-type Huh7 transduced with lentivirus particle pLV[Exp]-Puro-
529 CMV>{Perceval(ns)}:T2A:mCherry/3xNLS (Vector Builder) that were used for live imaging of
530 changes in ATP/ADP ratio within these cells, which directly correlates to cellular metabolic
531 activity.[58] LSEC cells were maintained in EBM-2 (Lonza) media with EGM-2 BulletKit (Lonza),
532 2% FBS and 1% penicillin/streptomycin (Gibco).

533 **Metabolic assays**: Effluents were collected at different timepoints (baseline, 24h, 48h
534 and 1-3 days recovery after washout) throughout the exposure to SNC80 or 1:1000 DMSO
535 vehicle. After treatment, the effluent was collected and analyzed for lactate and glutamate
536 production using the Lactate-Glo™ (Promega, #J5021) and Glutamate-Glo™ (Promega,
537 #J7021) assay kits respectively as per manufacturer protocols.
538 **Creatine kinase assay**: Creatine Kinase Colorimetric Activity Assay Kit (abcam,
539 #ab155901) was used as per manufacturer protocols. CK activity in experimental cells was
540 deduced from the colorimetric values obtained from the standard curve.
541 **Seahorse assay:** Four assays were run successively, one for each cell type – Caco-2,
542 Huh7, HUVEC, LSEC. Each cell type was plated on Agilent XFe24 plate to perform a Mitostress
543 Assay. Cells were added in all wells except A3, B1, C4 and D2 used for background
544 measurements. Cell concentrations were chosen to be 90% confluent on the day of experiment.
545 The days prior of experiment, the cartridge was hydrated in calibrant and incubated in non-CO2
546 incubator overnight. The day of experiment, cell media was changed to Seahorse XF medium to
547 which 1 mM pyruvate, 2 mM glutamine, and 10 mM glucose were added. Cells were allowed to
548 stabilize in this medium at 37C in a non-CO2 incubator for 1h. In the meantime, the drug
549 concentrations were prepared in Seahorse XF medium at a 10x concentration stock, so that
550 once injected on the cells, the concentration is diluted to 1x. Stock values were 1mM SNC80.
551 56uL of the drug (or media with DMSO vehicle for control wells) were loaded in port A of the
552 respective cartridge well. Port B was loaded with 62uL of 10uM Oligomycin, port C with 69uL of
553 10uM FCCP, and port D with 76uL of 5uM Antimycin A and 5uM rotenone. The Seahorse
554 instrument was programmed so that baseline OCR and ECAR measurements were taken
555 before the drugs were injected. Drugs were incubated for 2h, another measurement was taken,
556 and mitochondrial inhibitors were successively injected in the following order: Oligomycin,
557 FCCP, Rotenone. With the acquired measurements, we used the Agilent Wave software to
558 process the data.

559 **Cytotoxicity assay**: Cytotoxicity measurements on the Organ Chip effluents were
560 performed using the LDH-Glo™ (Promega, #J2380) as per manufacturer protocols.
561 **ATP/ADP ratio measurements**: Huh7 cells were transfected with a reporter that
562 enables direct measurements of cellular ATP:ADP ratio. The basal excitation spectrum of the
563 reporter protein was similar to that of YFP (peak around 490 nm) but it had an additional peak at
564 CFP wavelength (405 nm). As ATP levels decreased, more ADP can bind to the site,
565 decreasing the YFP/CFP ratio value. BioTek Cytation 5 Cell Imager (Agilent) was used to take
566 RFP, YFP and CFP images of each well every 20min for 180 minutes upon exposure to 100uM
567 SNC80 or 1:100 DMSO vehicle. Post processing of the images was performed using the open
568 source CellProfiler program.[59] We implemented the following pipeline to obtain quantitative
569 ATP/ADP ratio values: (1) Identify nuclei with RFP marker, (2) Define a cell as 4pixels around
570 the edge of the nuclei, (3) Measure cells YFP and CFP intensity and YFP/CFP ratio, (4) Count
571 cells per Image, (5) Track cells YFP and CFP intensity over the time course (0-3h with 20min
572 intervals), (6) Measure YFP/CFP ratio average **over all cells** per image and normalize to cell
573 count (7).
574 For the qualitative images, raw images were processed with ImageJ by using the image
575 calculator to divide yfp/cfp intensity of respective images. “Rainbow RGB” lookup table was
576 used to show the intensity changes. Tones towards the red show more intensity, higher
577 ATP/ADP ratio and higher metabolism.
578 **Organ Chips with Integrated Sensors:** To allow for live oxygen and
579 transepithelial\endothelial resistance (TEER) monitoring, we used our in-house developed and
580 fabricated microfluidic chips with integrated TEER and oxygen sensors. To mimic the *in vivo*-like
581 cell-cell interface on the models, a dual-channel PDMS microfluidic chip was used where the
582 apical channel is separated from the basal channel with a porous PDMS membrane. A pair of
583 TEER sensing electrodes where integrated on the apical side of the top channel and the basal
584 side of the bottom channel to measure the electrical resistance across the epithelium-

585 endothelium tissue interface. The O_2 sensing nanoparticles (OXNANO, PyroScience) were
586 integrated at four different locations in the chip: two in the apical channel and two in similar
587 locations in the bottom channel. This is to allow a fair representation of the whole chip oxygen
588 tension levels.

589 After fabrication, the chips were sterilized by plasma treatment and desiccated for 30
590 minutes. The polymeric surfaces of the membrane were then chemically functionalized using
591 ER1/ER2 buffers following Emulate^{TM} Inc. protocol and coated with extracellular matrix (ECM)
592 for 1.5-2 hours at 37°C. Gut Chip apical and basal channels were coated with 30 µg/ml
593 Collagen I (Advanced BioMatrix, Cat. no. 5005) and 100 µg/ml Matrigel (BD Biosciences) in cold
594 PBS. Liver Chip apical channel was coated with 30 µg/mL fibronectin (Corning, Cat. no.
595 356008) and 400 µg/mL Collagen I (Advanced BioMatrix, Cat. no. 5005) in cold DPBS, while the
596 basal channel was coated with 100 µg/mL Matrigel (BD Biosciences) and 200 µg/mL type I
597 collagen in cold DPBS. To create Gut Chip, HUVECs (6-8x10^6 cells/ml (P5)) were first seeded
598 on the bottom side of the permeable membrane in the basal channel and incubated for 2-3
599 hours at 37°C before seeding the Caco-2 cells (2-3x10^6 cells/ml (P78)) on the membrane in the
600 apical channel. Liver Chip was similarly created by seeding the LSEC (4-5x10^6 cells/ml (P3-8))
601 the first in the basal channel followed by seeding he Huh7 hepatocytes (2.5-3.5x10^6 cells/ml
602 (P5-15)) on the membrane in the apical channel The chips were then cultured under
603 continuous flow using the commercial culture module instrument (ZOË™ Culture Module,
604 Emulate Inc.,USA). The Gut Chips were maintained under continuous flow of 30µl/hr in the
605 apical and basal channels for 10 days before changing their respective media to differentiation-
606 promoting media (5% FBS in DMED apically and 0.5% FBS endothelial medium basally) for the
607 rest of the culture time. The Liver Chips were also maintained under continuous flow of growth
608 media at 30µl/hr in the apical and basal channels for 5-6 days before reducing the FBS content
609 to 5% in Huh7 media and 0.5% in LSEC media for inducing tissue differentiation.

610 **Human Organ Chip studies:** SNC80 was tested on the Gut Chip at day 16 of culture,
611 when the epithelium showed characteristics of matured, functional tissue and the Liver Chip was
612 tested after 7-10 days of culture. SNC80 [100μM] in the culture media was perfused through the
613 apical and basal channels of the chips at 30μl/hr, while the control chips were perfused with the
614 same culture media containing the compound's vehicle [0.5% DMSO] using the same flow
615 condition. The chips were treated with SNC80 for 48 hours before the drug was removed from
616 the media and the culture was continued for another 4 days. Both Liver and Gut Chips were
617 monitored at d-1, 0h, 3h, 24, 48h timepoints as well as day 1 and 3 after the drug washout for
618 oxygen consumption, TEER measurements, and effluent analysis. Fluorescence microscopy
619 was continuously performed from 0h throughout the treatment period and up to 3 days of
620 recovery. CellProfiler program was used to analyze ATP/ADP ratio as described above.
621 **Oxygen and TEER measurements on-chip:** Oxygen tension level measurements was
622 performed on-chip during the culture using FireSting®-O2 Optical Oxygen and Temperature
623 Meter (FSO2-C4, Pyroscience sensor technology, Germany) connected to Pryo Oxygen Logger
624 (V3.317©, Germany). TEER measurements were performed on-chip using our in-house
625 developed multiplexed TEER Tray and remotely measured from outside the incubator. A four-
626 point impedance measurement was taken on-chip periodically every 24 hours during the SNC80
627 treatment and recovery using the IviumSoft application (V4.97, Informer Technologies, Inc.). To
628 obtain the TEER of only the epithelial-endothelial tissue interface, the measured impedance at
629 100Hz was subtracted from the impedance at 100kHz and reported as the tissue impedance(Ω)
630 throughout the culture and in response to different stimuli as we reported previously.[60]
631 **DNA damage and proliferation assays**: The Click-IT™ EdU cell proliferation kit
632 (Thermofisher, #C10337) was used to assess cell proliferation in the formaldehyde-fixed chips
633 and DNA damage was assessed by staining anti-H2AX antibody (Novus Bio NB100-2280).

634 **Urea Assay**: Urea nitrogen was measured using a colorimetric assay (urea nitrogen
635 test, Stanbio Laboratory), whereby undiluted liver chip effluents were added to a 96 well plate
636 and mixed with the kit's working reagents as per manufacturer protocol.
637 **Albumin Assay**: Liver albumin production was measured using an enzyme-linked
638 immunosorbent assay (Bethyl Laboratories). Liver Chip effluents were diluted 1:100 in buffer
639 before being plated in the kit's 96 well plate, aside from standard wells with dilution series of
640 known albumin concentration solution. We followed manufacturer protocol to perform the
641 sandwich ELISA assay and measure absorbance at 450nm.
642 **Porcine heart *ex vivo* perfusion studies:** After induction of anesthesia and preparation
643 for clean, non-survival surgery, a median sternotomy was performed followed by longitudinal
644 incision in the pericardium to expose the heart and the great vessels. Following blunt dissection
645 and exposure of the vena cava, aorta and the brachycephalic artery, the superior vena cava,
646 and azygos vein was ligated and divided. The brachycephalic artery was catheterized for
647 infusion of cardioplegia solution. The inferior vena cava was clamped and divided proximal to
648 the clamp. Two or three pulmonary arteries were incised for decompression of the left side of
649 the heart. The aorta was immediately clamped and 10-15 ml/kg of body weight of cold (2-4°C)
650 cardioplegia solution (del Nido without lidocaine, 3 L) was infused at a pressure of 70-80mmHg
651 to stop the heart. Cold 4°C saline and ice were poured over the heart and the accumulated
652 fluids from the thoracic cavity were removed by suction. Following cessation of myocardial
653 function, the heart was removed from the chest by further dissection and division of the
654 pulmonary vessels and aorta distal to the clamp. The heart was cooled in a surgical bowl with
655 cold saline for inspection and preparation for perfusion. All procedures were conducted under
656 the UT Health San Antonio approved Institutional Animal Care and Use Committee (IACUC)
657 protocol 20210080AR.
658 After the heart was removed and placed in a surgical bowl, the aorta and the coronary
659 sinus were cannulated using sterile zip ties. The heart was placed into the VP.S ENCORE®

660 perfusion device filled with 3 L of Krebs-Henseleit buffer supplemented with 20PEG and
661 hemoglobin-based oxygen carrier (HBOC; Hemoglobin Oxygen Therapeutics, LLC, Souderton,
662 PA). The heart was perfused with a pressure of approximately <20 mmHg resulting in a
663 coronary perfusate flow of 50-100 mL/min at a 20-23°C temperature. Hearts were immediately
664 treated with 3 mL of 3% lactic acid containing 135 mg of SNC80 (100 μM final concentration),
665 administered through the arterial line followed by the 3 mL of Krebs-Henseleit flush. Post drug
666 administration, the heart continued to be perfused for additional 6 hours.

667 Two oxygen probes (Pyro FireSting™) collected oxygen partial pressure (mmHg) data of
668 the solution before entering the coronary arteries (arterial) and after exiting the cannulated
669 pulmonary artery (venous), whereas flow was measured using the Sensirion flow meter. Oxygen
670 consumption was captured using the following formula, (([O_2]a- [O_2]v)/100 * Q)/heart weight) *
671 100. [O_2]a and [O_2]v are defined as oxygen content of arterial and venous perfusate
672 respectively. [O_2] was calculated as (1.34 * Hb* SO_2) + (K * pO_2); where 1.34 is mL O_2 / Hb
673 (g), Hb is the concentration of hemoglobin measured in g/dL, SO_2 is the oxygen saturation ratio
674 calculated using the equation developed by Severinghaus,[61] K is the oxygen solubility
675 coefficient adjusted for the perfusate temperature at every data point, pO_2 is the partial pressure
676 of oxygen in mmHg for the perfusate sample, and Q is coronary flow in mL/min.

677 After preservation, hearts were placed on a Langendorff system with a perfusate mixture
678 of 1:1 porcine blood and Krebs-Henseleit buffer. Myocardial oxygen consumption
679 (MVO_2 mLO_2 /min / 100g) was calculated during an initial 30 min of rewarming stage (before
680 defibrillation) and after defibrillation using two oxygen probes (Pyro FireSting™, placed in
681 arterial and venous effluent). Oxygen consumption was [53]calculated using the same approach
682 described for the VP.S ENCORE® perfusion stage. The left ventricular function was expressed
683 as dP/dT (mmHg/sec) measured by placing a pressure catheter (Millar, 5F) in the left ventricle.
684 Data was analyzed using PowerLab (LabChart 8.1.16) blood pressure analyzer. Data was

685 selected from the left ventricular pressure waveform as the average of 30 beats after
686 stabilization (approx. 30 minutes after defibrillation). Contractility after ionotropic support was
687 measured less than 5 minutes after administration of epinephrine (0.5mg injected arterial). End
688 diastolic pressure of the left ventricle was maintained 5.14 +/- 1.89 mmHg through administering
689 perfusate directly into the left ventricle through the pulmonary veins and venting to
690 atmosphere.

691 ECG data were obtained through the placement of leads on the apex (positive), right
692 atrial appendage (negative), and aortic root (ground). Data was collected through the PowerLab
693 system and 30-second time intervals were selected for all groups before the flush, before
694 defibrillation, at native contraction, and after epinephrine drug administration. The ECG
695 amplitude (mV) was analyzed using LabChart Pro (v8.1.19) peak analysis detection at
696 approximate time points 10min (before flush) and 30min (before defibrillation) to detect the
697 average amplitude of electrical activity without full contraction. LabChart Pro (v8.1.19) ECG
698 Analysis detection was used at time points 35min (Epinephrine) and 60min (Native) to detect
699 the average amplitude of the QRS complex with contraction. The native QRS Interval (s) and ST
700 Height (mV) was averaged over a 30-second time interval using LabChart Pro (v8.1.19) ECG
701 Analysis.

702 After the experiment, biopsy tissue samples were collected from SNC80 and vehicle-
703 treated samples for RNA-Seq analysis and histological evaluation. Total RNA from cardiac
704 tissue biopsies (2.5 mm) were extracted following the RNeasy Mini kit (Qiagen) according to the
705 manufacturer's instructions. The concentration of total RNA was evaluated and measured at
706 260/280nm by spectrophotometer (NanoVue Plus, GE Healthcare). Synthesis of cDNA was
707 performed from 0.5 µg of total RNA, which was reverse transcribed using (iScript cDNA
708 Synthesis Kit, Bio-Rad) according to the manufacturer's instructions. Gene-specific pre-
709 designed oligonucleotide primers were purchase from Sigma. qRT-PCR was done using
710 SsoAdvanced Universal SYBR Green Supermix and SFX96 Touch real time PCR detection

711 system (Bio-Rad, T100 Thermal Cycler). The cycling parameters were as follows: initial
712 denaturation 95°C, 2 min; denaturation 95°C, 5 s; annealing/extension 60°C, 30 s; number of
713 cycles 40; melt curve 65°-95°C (0.5°C increments). The comparative CT (2-ΔΔCT) method was
714 used for all quantification. Values were normalized to the Gapdh housekeeping gene.
715 Myocardial degeneration, myocardial hemorrhage, interstitial edema, and endothelial changes
716 were semi-quantitatively graded from histology images on a scale of 0-3 by a clinician blinded to
717 sample and intervention using previously published guidelines.[62]

718 **Porcine limb *ex vivo* perfusion studies:** Hindlimbs (N=8) were procured via protocol
719 tissue sharing at the Joint Base San Antonio Clinical Investigation and Research Support
720 (CIRS) building, following IV Pentobarbital euthanasia, 100 mg/kg from a host protocol. Host
721 protocol animals were treated with the same surgical manipulations and no chemicals or drugs
722 were introduced experimentally prior to euthanasia. Following euthanasia, a curvilinear incision
723 was made around the hindlimb circumferentially. Subsequently, the neurovascular pedicle in the
724 medial hindlimb was identified and carefully dissected out to preserve the vascular bundle. The
725 pedicle was then divided at the origin of the artery and vein to preserve maximal length of the
726 vessels. Hindlimb bone was separated using a Gigli Saw. Hindlimbs were cannulated through
727 the femoral artery and underwent immediate arterial flush with up to 200-400 mL heparinized-
728 saline solution (10,000 units of heparin per 1L of saline), until venous outflow was clear.
729 Additionally, the femoral vein was cannulated for measurement and collection of venous outflow
730 samples.

731 Limbs were divided into two groups, control (N=3) and experimental SNC80 (N=5). All
732 hindlimbs were connected to the ENCORE® head for perfusion via the cannulated femoral
733 artery. The femoral vein was cannulated for obtaining venous samples. Hindlimbs were
734 perfused with oxygenated Krebs-Henseleit (KH) at ambient temperature. Arterial and venous
735 pO2 were assessed hourly using a commercial blood gas analyzer (ALB1000 by Radiometer,
736 Brea, California USA). Oxygen consumption was calculated from A-V differences obtained from

737 arterial and venous blood gas readings. After 3 hours of perfusion (baseline), torpor inducing
738 compound SNC80 (44.96 µg/ml) was administered via the femoral artery to the experimental
739 group (SNC80) (N=5) and an equal volume of the sham vehicle to the control limbs (N=3)
740 followed by and additional 3 hours of perfusion (drug). The hind limbs were then removed from
741 the perfusor and flushed with fresh KH perfusate and replaced into the perfusor containing fresh
742 KH solution (flush). The perfusion then resumed for an additional 6 hours. Relative metabolic
743 rate was defined as the oxygen consumption rate over time, normalized to baseline
744 measurements. The hindlimbs were weighed pre and post-perfusion. Biopsy tissue samples
745 were taken at baseline (pre-ENCORE®), and before and after the administration of the SNC80
746 compound for RNA-Seq analysis and histological evaluation.
747 Biopsies for histopathology were obtained superficially from the rectus femoris muscle
748 bundle immediately after amputation and then 24 hours after the perfusion period. Biopsies
749 were stored in 10% formalin for 24 hours and then stored for 3 days in 70% ethanol and
750 embedded in paraffin. The samples were sectioned into 5µm slides and stained with
751 hematoxylin and eosin (H&E) to evaluate tissue morphology, intracellular distance, muscle
752 bundle area, and Periodic Acid-Schiff to evaluate glycogen content. Histological analysis was
753 performed by visualizing slides under a light microscope (AM Scope T670Q, Irvine, California)
754 and capturing images using a high-definition camera (AM Scope Model# MU2003B1, Irvine,
755 California). From each slide, 10 digital images from randomly selected fields were obtained at
756 10x magnification. The images were de-identified and evaluated for intracellular distance,
757 muscle bundle area and glycogen content by two independent reviewers using Image J
758 software (v.1.51.).
759 **Statistical analysis.** All graphing and statistical analyses were performed with Prism 9
760 (GraphPad Software Inc., La Jolla, CA, USA) with a (two-sided) significance level of 0.05.
761 Statistical tests and corrections for multiple comparisons are described in each figure panel.
762

Data availability statement

The proteomics data reported in this paper have been deposited in the Mass Spec Interactive Virtual Environment, MassIVE, (accession no. MSV000091410). All other data are available within the paper and its Supplementary Information files.

Software availability statement

A custom Python script was used to automatically count heart beat in *Xenopus* tadpoles. This code can be accessed on GitHub: https://github.com/k-shcherb/heart_seg.

Acknowledgements

The authors gratefully acknowledge funding from the Army Research Office/DARPA under Cooperative Agreement Number W911NF-19-2-0027. The views and conclusions contained in this document are those of the authors and should not be interpreted as representing the official policies, either expressed or implied, of the Army Research Office/DARPA or the U.S. Government. The U.S. Government is authorized to reproduce and distribute reprints for Government purposes notwithstanding any copyright notation herein. M.P.O. acknowledges financial support from the Margarita Salas postdoctoral grant (UNI/551/2021). We thank E. Switzer for *Xenopus* embryo fertilization; R. Colon, S. Sundar, and E. Lederer for *Xenopus* embryo husbandry and transport organization; members of the Levin Lab, Tufts University for useful discussions; and R. Gould for help with database extraction. Image analysis workflows were created in consultation with D. Stirling and B. Cimini of the Broad Institute Imaging Platform.

Author Contributions

R.N., M.Su., and D.E.I. conceived of and directed the work. M.M.S., H.F., E.G., A.K., S.K., M.P.O., K.She., and T.L. performed *Xenopus* studies with guidance from R.N. and M.Lev. R.M.

developed and maintained engineered components for *Xenopus* assays. H.F., M.M.S., A.K., M.P.O., and T.T. analyzed *Xenopus* data. T.L. and M.Lew. performed MALDI-TOF experiments and analyzed the data. B.C., K.P., and Z.I. performed *in vitro* and Organ Chip studies and analyzed data with guidance from A.M.S. S.M. and K.Shc. designed, assembled, and maintained custom microscopy equipment for Organ Chip imaging. K.Shc. analyzed imaging data from tadpole and *in vitro* experiments. S.L. oversaw compound management and material transfers. J.M. designed novel chemical entities. Porcine heart experiments were conceived and directed by R.V. and L.B and experiments were designed and interpreted by R.V., L.B., and K.A. Porcine heart data analysis was performed by R.V., L.B., K.A, E.C., R.L., I.C., Z.M., and D.D.C. Porcine heart data was acquired by K.A, E.C., R.L., I.C., and Z.M. Porcine limb studies were conceived and directed by R.V., L.B., E.W., and T.P. Porcine limb surgeries were performed by J.Y., O.P., and J.S. Porcine limb sampling and data analysis were performed by R.V., L.B., J.P., D.W., Z.H., C.H. and J.C.H. M.M.S., B.C., K.P., Z.I., T.L., K.A., R.N. and D.E.I. drafted the manuscript and all authors reviewed and provided critical input for the manuscript.

Competing Interests

D.E.I. is a founder, board member and Scientific Advisory Board chair of, and holds equity in, Emulate Inc. M.Le., R.N., M.M.S., E.G., T.T., and D.E.I are inventors on a relevant patent application held by Harvard University (PCT/US2021/012626). R.N., E.G., M.Le., and D.E.I. hold equity in Unravel Biosciences, Inc.; R.N. and D.E.I. are members of its board of directors; M.Le. and D.E.I. are members of its scientific advisory board; and R.N. and E.G. are current employees of the company. R.V., L.B., K.A, E.C., R.L., I.C., and Z.M are employees of Vascular Perfusion Solutions. D.E.I. is a member of its scientific advisory board. The remaining authors declare no competing interests.

References

1. Vela, R. J., Jessen, M. E. & Peltz, M. Ice, ice, maybe? Is it time to ditch the igloo cooler? Benefits of machine perfusion preservation of donor hearts. *Artificial Organs* vol. 44 220–227 Preprint at https://doi.org/10.1111/aor.13599 (2020).
2. Petrenko, A. *et al.* Organ Preservation into the 2020s: The Era of Dynamic Intervention. *Transfusion Medicine and Hemotherapy* vol. 46 151–172 Preprint at https://doi.org/10.1159/000499610 (2019).
3. Guibert, E. E. *et al.* Organ preservation: Current concepts and new strategies for the next decade. *Transfusion Medicine and Hemotherapy* vol. 38 125–142 Preprint at https://doi.org/10.1159/000327033 (2011).
4. Andrijevic, D. *et al.* Cellular recovery after prolonged warm ischaemia of the whole body. *Nature* (2022) doi:10.1038/s41586-022-05016-1.
5. Tessier, S. N. *et al.* Partial freezing of rat livers extends preservation time by 5-fold. *Nat Commun* **13**, 4008 (2022).
6. Hrvatin, S. *et al.* Neurons that regulate mouse torpor. *Nature* **583**, 115–121 (2020).
7. Takahashi, T. M. *et al.* A discrete neuronal circuit induces a hibernation-like state in rodents. *Nature* **583**, 109–114 (2020).
8. Dou, M., Lu, C. & Rao, W. Bioinspired materials and technology for advanced cryopreservation. *Trends in Biotechnology* vol. 40 93–106 Preprint at https://doi.org/10.1016/j.tibtech.2021.06.004 (2022).
9. Blackstone, E., Morrison, M. & Roth, M. B. H2S induces a suspended animation-like state in mice. *Science (1979)* **308**, 518 (2005).
10. Beal, E. W. *et al.* [D-Ala 2 , D-Leu 5] Enkephalin Improves Liver Preservation During Normothermic Ex Vivo Perfusion. *Journal of Surgical Research* **241**, 323–335 (2019).
11. Ratigan, E. D. & McKay, D. B. Exploring principles of hibernation for organ preservation. *Transplantation Reviews* vol. 30 13–19 Preprint at https://doi.org/10.1016/j.trre.2015.08.002 (2016).
12. Schultz, J. J., Hsu, A. K. & Gross, G. J. *Ischemic Preconditioning and Morphine-Induced Cardioprotection Involve the Delta (d)-Opioid Receptor in the Intact Rat Heart*. *Journal of Molecular and Cellular Cardiology* vol. 29 (1997).
13. Rawls, S. M., Hewson, J. M., Inan, S. & Cowan, A. Brain delta2 opioid receptors mediate SNC-80-evoked hypothermia in rats. *Brain Res* **1049**, 61–69 (2005).
14. Horiuchi, T. *et al.* The Effects of the δ-Opioid Agonist SNC80 on Hind-Limb Motor Function and Neuronal Injury After Spinal Cord Ischemia in Rats. *Anesth Analg* **99**, 235–240 (2004).
15. Sperry, M. M. *et al.* Enhancers of host immune tolerance to bacterial infection discovered using linked computational and experimental approaches. *Advanced Science* (2022).
16. Novak, R. *et al.* Target-agnostic discovery of Rett Syndrome therapeutics by coupling computational network analysis and CRISPR-enabled in vivo disease modeling. *bioRxiv* (2022) doi:10.1101/2022.03.20.485056.
17. Schmitt, S. M., Gull, M. & Brändli, A. W. Engineering Xenopus embryos for phenotypic drug discovery screening. *Adv Drug Deliv Rev* **69–70**, 225–246 (2014).
18. Sullivan, K. G. & Levin, M. Inverse drug screening of bioelectric signaling and neurotransmitter roles: Illustrated using a Xenopus tail regeneration assay. *Cold Spring Harb Protoc* **2018**, 154–163 (2018).
19. Giroud, S. *et al.* Lipidomics reveals seasonal shifts in a large-bodied hibernator, the brown bear. *Front Physiol* **10**, (2019).

20. Kolomiytseva, I. K. Lipids in mammalian hibernation and artificial hypobiosis. *Biochemistry (Moscow)* vol. 76 1291–1299 Preprint at https://doi.org/10.1134/S0006297911120029 (2011).
21. Soeters, M. R. *et al.* Muscle acylcarnitines during short-term fasting in lean healthy men. *Clin Sci* **116**, 585–592 (2009).
22. Welinder, K. G. *et al.* Biochemical foundations of health and energy conservation in hibernating free-ranging subadult brown bear ursus arctos. *Journal of Biological Chemistry* **291**, 22509–22523 (2016).
23. Otis, J. P., Sahoo, D., Drover, V. A., Yen, C. L. E. & Carey, H. V. Cholesterol and lipoprotein dynamics in a hibernating mammal. *PLoS One* **6**, (2011).
24. Jones, L. L., McDonald, D. A. & Borum, P. R. Acylcarnitines: Role in brain. *Progress in Lipid Research* vol. 49 61–75 Preprint at https://doi.org/10.1016/j.plipres.2009.08.004 (2010).
25. Petrov, A., Kasimov, M. & Zefirov, A. Brain Cholesterol Metabolism and Its Defects: Linkage to Neurodegenerative Diseases and Synaptic Dysfunctio. *Acta Naturae* **8**, 58–73 (2016).
26. Chu Sin Chung, P. *et al.* Delta opioid receptors expressed in forebrain GABAergic neurons are responsible for SNC80-induced seizures. *Behavioural Brain Research* **278**, 429–434 (2015).
27. Veraza, R. *et al.* (872) Preclinical Evaluation of the VP.S ENCORE^{TM} Cardiac Preservation Device. *The Journal of Heart and Lung Transplantation* **42**, S379 (2023).
28. Andrijauskaite, K. *et al.* (399) Novel Portable Hypothermic Perfusion Preservation Device Enhances Cardiac Output of Donated Human Hearts. *The Journal of Heart and Lung Transplantation* **42**, S188 (2023).
29. Kaltenborn, A. *et al.* Ex vivo limb perfusion for traumatic amputation in military medicine. *Mil Med Res* **7**, (2020).
30. Ralphe, J., Segar, J., Schutte, B. & Scholz, T. Localization and function of the brain excitatory amino acid transporter type 1Bin cardiac mitochondria. *J Mol Cell Cardiol* **37**, 33–41 (2004).
31. Maiolino, M. *et al.* Essential role of the Na+-Ca2+ exchanger (NCX) in glutamate-enhanced cell survival in cardiac cells exposed to hypoxia/reoxygenation. *Sci Rep* **7**, 13073 (2017).
32. Magi, S. *et al.* Glutamate-induced ATP synthesis: Relationship between plasma membrane Na+/Ca2+ exchanger and excitatory amino acid transporters in brain and heart cell models. *Mol Pharmacol* **84**, 603–614 (2013).
33. Magi, S., Piccirillo, S. & Amoroso, S. The dual face of glutamate: from a neurotoxin to a potential survival factor—metabolic implications in health and disease. *Cellular and Molecular Life Sciences* vol. 76 1473–1488 Preprint at https://doi.org/10.1007/s00018-018-3002-x (2019).
34. Magi, S., Piccirillo, S. & Amoroso, S. The dual face of glutamate: from a neurotoxin to a potential survival factor—metabolic implications in health and disease. *Cell. Mol. Life Sci.* **76**, 1473–1488 (2019).
35. Chiba-Falek, O., Gottschalk, W. K. & Lutz, M. W. *The Effects of the TOMM40 Poly-T Alleles on Alzheimer's Disease Phenotypes*. (2018).
36. Yang, Y. *et al.* Mitochondrial UQCC3 Modulates Hypoxia Adaptation by Orchestrating OXPHOS and Glycolysis in Hepatocellular Carcinoma. *Cell Rep.* **33**, 108340 (2020).
37. Klepinina, L. *et al.* Colon cancer cell differentiation by sodium butyrate modulates metabolic plasticity of Caco-2 cells via alteration of phosphotransfer network. *PLoS One* **16**, e0245348 (2021).
38. Mookerjee, S. A. & Brand, M. D. Measurement and analysis of extracellular acid production to determine glycolytic rate. *J. Vis. Exp.* **2015**, 1–9 (2015).

39. Gaude, E. *et al.* NADH Shuttling Couples Cytosolic Reductive Carboxylation of Glutamine with Glycolysis in Cells with Mitochondrial Dysfunction. *Mol. Cell* **69**, 581–593.e7 (2018).
40. Fendt, S. M. *et al.* Reductive glutamine metabolism is a function of the α-ketoglutarate to citrate ratio in cells. *Nat. Commun.* **4**, 2236 (2013).
41. Posho, L., Delbos-Bocage, L., Gueylard, D., Farinotti, R. & Carbon, C. Effects of Salmonella typhimurium infection and ofloxacin treatment on glucose and glutamine metabolism in Caco-2/TC-7 cells. *Antimicrob. Agents Chemother.* **42**, 2950–2955 (1998).
42. Costa, C., Huneau, J. F. & Tomé, D. Characteristics of L-glutamine transport during Caco-2 cell differentiation. *Biochim. Biophys. Acta - Biomembr.* **1509**, 95–102 (2000).
43. De Bock, K. *et al.* XRole of PFKFB3-driven glycolysis in vessel sprouting. *Cell* **154**, 651–663 (2013).
44. Wan, H. *et al.* NCX1 coupled with TRPC1 to promote gastric cancer via Ca2+/AKT/β-catenin pathway. *Oncogene* (2022) doi:10.1038/s41388-022-02412-9.
45. Ingber, D. E. Human organs-on-chips for disease modelling, drug development and personalized medicine. *Nature Reviews Genetics* vol. 23 467–491 Preprint at https://doi.org/10.1038/s41576-022-00466-9 (2022).
46. Si, L. *et al.* A human-airway-on-a-chip for the rapid identification of candidate antiviral therapeutics and prophylactics. *Nat Biomed Eng* (2021) doi:10.1038/s41551-021-00718-9.
47. Kim, H. J., Li, H., Collins, J. J. & Ingber, D. E. Contributions of microbiome and mechanical deformation to intestinal bacterial overgrowth and inflammation in a human gut-on-a-chip. *Proc Natl Acad Sci U S A* **113**, E7–E15 (2016).
48. Choi, Y. Y., Kim, J., Lee, S. H. & Kim, D. S. Lab on a chip-based hepatic sinusoidal system simulator for optimal primary hepatocyte culture. *Biomed Microdevices* **18**, (2016).
49. Ewart, L. *et al.* Qualifying a human Liver-Chip for predictive toxicology: Performance assessment and economic implications. *bioRxiv* 2021.12.14.472674 (2021) doi:10.1101/2021.12.14.472674.
50. Maassen, H. *et al.* Hydrogen sulphide-induced hypometabolism in human-sized porcine kidneys. *PLoS One* **14**, (2019).
51. Kon, N. *et al. Na + /Ca 2+ Exchanger Mediates Cold Ca 2+ Signaling Conserved for Temperature-Compensated Circadian Rhythms*. *Sci. Adv* vol. 7 http://advances.sciencemag.org/ (2021).
52. Shah Amran, M., Homma, N. & Hashimoto, K. *Pharmacology of KB-R7943: A Na +-Ca 2+ Exchange Inhibitor-Sion Arrhythmia-KB-R7943-Na +-Ca 2+ Exchange (NCX1-3)-NCX Inhibitors-Ni 2+-SEA0400-SN-6*. (2003).
53. Schafer, C. *et al. Role of the Reverse Mode of the Na / Ca Exchanger in Reoxygenation-Induced Cardiomyocyte Injury*. *Cardiovascular Research* vol. 51 www.elsevier.com/locate/cardiores (2001).
54. Headrick, J. P., See Hoe, L. E., Du Toit, E. F. & Peart, J. N. Opioid receptors and cardioprotection-'opioidergic conditioning' of the heart Correspondence LINKED ARTICLES. *Br J Pharmacol* **172**, 2026–2050 (2015).
55. Pugsley, M. K. The diverse molecular mechanisms responsible for the actions of opioids on the cardiovascular system. *Pharmacol Ther* **93**, 51–75 (2002).
56. Bankhead, P. *et al.* QuPath: Open source software for digital pathology image analysis. *Sci Rep* **7**, (2017).
57. Goto-Inoue, N., Kashiwagi, A., Kashiwagi, K. & Mori, T. Metabolomic approach for identifying and visualizing molecular tissue markers in tadpoles of Xenopus tropicalis by mass spectrometry imaging. *Biol Open* **5**, 1252–1259 (2016).
58. Berg, J., Hung, Y. P. & Yellen, G. A genetically encoded fluorescent reporter of ATP:ADP ratio. *Nat. Methods* **6**, 161–166 (2009).

59. Stirling, D. R. *et al.* CellProfiler 4: improvements in speed, utility and usability. *BMC Bioinformatics* **22**, (2021).
60. Henry, O. Y. F. *et al.* Organs-on-chips with integrated electrodes for trans-epithelial electrical resistance (TEER) measurements of human epithelial barrier function. *Lab Chip* **17**, 2264–2271 (2017).
61. Severinghaus, J. W. *Simple, Accurate Equations for Human Blood 02 Dissociation Computations*. (1979).
62. Trahanas, J. M. *et al.* Achieving 12 Hour Normothermic Ex Situ Heart Perfusion: An Experience of 40 Porcine Hearts. *ASAIO Journal* **62**, 470–476 (2016).

976 ## Figure Legends

977 **Figure 1. SNC80 treatment in *Xenopus* tadpoles. a.** Swimming activity of *Xenopus*
978 during 100μM SNC80 or vehicle treatment. Data represent the mean±SD of n=3 replicates, with
979 10 tadpoles per replicate. **b.** Oxygen consumption rate for *Xenopus* treated with SNC80 or
980 vehicle controls. N=5 medium only, n=7 vehicle and n=9 SNC80, with each data point
981 representing the cumulative oxygen consumption for 5 tadpoles. **c.** Heart rate in SNC80 and
982 vehicle-treated *Xenopus* (n=10 tadpoles/group). Statistical comparisons were performed using a
983 Brown-Forsythe and Welch ANOVA test with a Dunnett correction for multiple comparisons (**b**)
984 and a 2-way ANOVA (treatment x timepoint) with Tukey correction for multiple comparisons (**c**).
985 Bar plots show the mean±SD of each group.

986 **Figure 2. SNC80 uptake and activity at the delta opioid receptor. a.** Distribution of
987 SNC80 in *Xenopus* tadpoles after 1 and 2 hours of compound exposure. **b.** Uptake of SNC80 in
988 the tadpole skeletal muscle, GI tract, and gills at 1 and 2 hours of exposure. **c.** Levels of
989 acylcarnitine and cholesterol ester in the skeletal muscle, brain, and cardiac tissue after 1 hour
990 of SNC80 treatment. *In vivo* distributions of SNC80 and lipid levels measured from N=5
991 tadpoles per condition; N=3 sections/slide. **d.** Oxygen consumption in *Xenopus* tadpoles treated
992 with SNC80, the delta opioid antagonist naltrindole, or a combination of SNC80 and naltrindole.
993 N=3 replicates/group with each data point representing the cumulative oxygen consumption
994 from 5 tadpoles. Statistical comparisons were performed using a two-way ANOVA (time x tissue
995 region) with Sidak's correction for multiple comparisons (**b**), multiple unpaired t-tests for each
996 tissue region with FDR correction (**c**), and a Welch ANOVA test with Dunnett correction for
997 multiple comparisons between vehicle and each treatment group (**d**). Bar plots show the
998 mean±SD of each group.

999 **Figure 3. Design and *in vivo* screening of novel analog WB3. a.** Molecular structures
1000 for SNC80 and novel compound WB3. **b.** Percent specific binding of the delta opioid receptor

1001 radioligand [3H]-DADLE in the presence of SNC80 and WB3. **c.** Swimming activity of *Xenopus*
1002 during 100μM WB3, SNC80, or vehicle treatment. Data represent the mean±SD of n=2
1003 replicates, with 10 tadpoles per replicate. **d.** Oxygen consumption rate for *Xenopus* treated with
1004 WB3 or vehicle controls. N=4 vehicle and n=3 WB3, with each data point representing the
1005 cumulative oxygen consumption for 5 tadpoles. **e.** Heart rate in WB3 and vehicle-treated
1006 *Xenopus* (n=10 tadpoles/group). Statistical comparisons were performed using Welch's
1007 unpaired t-test (**d**) and a two-way ANOVA (group x timepoint) with Sidak correction for multiple
1008 comparisons (**e**). Bar plots show the mean±SD of each group.

1009 **Figure 4. Preservation of porcine cardiac grafts with SNC80 over 6 hours. a.**
1010 Oxygen consumption for vehicle and SNC80-treated cardiac grafts perfused in the VP.S
1011 ENCORE® device (n=3 hearts/group). **b.** Oxygen consumption during cardiac reperfusion on the
1012 Langendorff system before defibrillation (n=3 vehicle and n=3 SNC80 hearts). **c.** Oxygen
1013 consumption measured on the Langendorff system after defibrillation (n=3 vehicle and n=3
1014 SNC80 hearts). **d.** Left ventricle (LV) contractility and relaxation before and after defibrillation
1015 and tissue exposure to epinephrine (n=3 vehicle and n=2 SNC-treated hearts). **e.** Gene
1016 expression analysis of heart biopsy samples for vehicle and SNC80-treated cardiac grafts (n=2
1017 hearts/group; 3 technical replicates each). **f.** Light microscopic views of H&E-stained histological
1018 sections of heart biopsies (20x magnification) after 6 hours of perfusion and quantification of
1019 myocardial degeneration (MD), myocardial hemorrhage (MH), interstitial edema (IE), and
1020 endothelial changes (EC). Statistical comparisons were performed using multiple unpaired t-
1021 tests between SNC80 and vehicle-treated cardiac grafts (**a,b,c**), two-way ANOVA with Sidak
1022 correction for multiple comparisons between SNC80 and vehicle-treated cardiac grafts (**d,f**), and
1023 unpaired t-tests between SNC80 and vehicle for each gene of interest (**e**). Data represent the
1024 mean±SD.

1025 **Figure 5. SNC80 treatment in human Organ Chips. a.** Monitoring changes in O_2 levels
1026 in human Gut (dotted lines; n=6 Chips/group) or Liver (straight lines; n=15-16 Chips/group)
1027 Chips throughout the treatment with 100 μM SNC80 (0-48h) and recovery (48-120h) versus
1028 vehicle control Chip. **b.** Graph showing the quantitative drop in ATP/ADP ratio of Liver Chip
1029 treated for 48h with 100μM SNC80 or Vehicle control as well as 2 days recovery after drug
1030 washout (n=5 control and n=3 SNC80 Chips). Statistical comparisons were performed using
1031 multiple unpaired t-tests for each timestamp with multiple comparison between control and
1032 treated cells. Data represent the mean±SD.
1033

1034 ## Tables

1035 **Table 1. SNC80 protein binding targets identified by thermal proteome profiling.**
1036

1037 ## Supplemental Figure Legends

1038 **Figure S1. Metabolic measurements in SNC80-treated *Xenopus* embryos.** Oxygen
1039 consumption rate in *Xenopus* embryos treated with SNC80 (n=3-4 replicates/group). Statistical
1040 comparisons were performed using a Brown-Forsythe and Welch ANOVA test with Dunnett
1041 correction for multiple comparisons between untreated and each treatment group. Data
1042 represent the mean±SD.

1043 **Figure S2. Preservation of whole porcine limbs with SNC80. a.** The relative
1044 metabolic rate at baseline is not statistically significantly different between control (n=3) and
1045 SNC80 (n=5) injected limbs. Metabolic rate is reduced during the treatment and washout
1046 phases for SNC80 relative to controls. **b.** Mean muscle bundle area between T0 before SNC80
1047 administration and at T3 after SNC80 administration and histographs of limb biopsy (20x
1048 magnification) at T0 before SNC80 administration and T3 after SNC80 administration. Muscle
1049 bundle area is not affected by the administration of SNC80. **c.** Optical density between T0

1050 before SNC80 administration and at T3 after SNC80 administration and histographs of limb
1051 biopsy (20x magnification) at T0 before SNC80 administration and T3 after SNC80
1052 administration. Optical density is not affected by the administration of SNC80. **d.** Mean
1053 intracellular distance during T0 before SNC80 administration versus T3 after SNC80
1054 administration and histographs of limb biopsy (10x magnification) at T0 before SNC80
1055 administration and T3 after SNC80 administration. Red arrows indicate intracellular distance
1056 measured. Intracellular distance increases after the administration of SNC80. Statistical
1057 comparisons were performed using a mixed-effects analysis with a Sidak's test for multiple
1058 comparisons (a) and Welch's t-test (b-d). Data represent the mean±SD.

1059 **Figure S3. SNC80 treatment in cell culture and Organ Chip systems. a.** Oxygen
1060 consumption rate (OCR) and mitochondrial ATP production obtained with Seahorse
1061 measurements for Caco-2 intestinal epithelium (filled circle), HUVEC (empty circles), Huh7 liver
1062 epithelium (filled squares) and LSEC (empty squares) after 2h 100μM SNC80 treatment (n=3-4
1063 biological replicates/cell type). Values are normalized to their respective vehicle controls. **b.**
1064 Graph showing the quantitative drop in ATP/ADP ratio of Huh7 cells treated with 100μM SNC80
1065 (n=2 control and n=3 SNC80 biological replicates). Statistical comparisons were performed
1066 using a two-way ANOVA with Dunnett correction with multiple comparison control vs treatment
1067 for each dataset. Data represent the mean±SD.

1068 **Figure S4. Metabolic measurements in gut and liver cultures treated with SNC80.**
1069 **a**. Normalized percent cytotoxicity for Caco2 intestinal epithelial cells (filled circles) or HUVECs
1070 (empty circles) as well as Huh7 liver epithelium (filled squares) or LSECs (empty squares) after
1071 2 hours of exposure to 100μM SNC80 (n=3 biological replicates/cell type). **b.** Normalized ECAR,
1072 glutamate, and creatine kinase (CK) activity in for Caco2 intestinal epithelial cells (filled circles)
1073 and HUVECs (empty circles) as well as Huh7 liver epithelium (filled squares) and LSECs (empty
1074 squares) (n=3-6 biological replicates/measurement/cell type). Statistical comparisons were

1075 performed using a two-way ANOVA with Dunnett correction with multiple comparison control vs
1076 treatment for each dataset (a,b). Data represent the mean±SD.

1077 **Figure S5. Characterization of human Gut and Liver Chips with integrated sensing**
1078 **technology. a.** Illustration of the sensor-integrated OOC unit connected to reservoir pod for
1079 automatic operation of fluid flow using pneumatic pressure (left). Inset shows a schematic of the
1080 top and bottom views of the sensor-chip-PCB compartment showing locations of TEER
1081 electrodes and O_2 sensors in the apical and basal channels. Four O_2 sensing spots were added
1082 to the channels - two in the top and two in the bottom channels for across the chip
1083 measurement. Electrode connectors are necessary for remote TEER sensing. **b.** Phase contrast
1084 images of Caco-2 cells seeded on sensor-chip at day 1, and 10 of culture (top) and Huh7 cells
1085 seeded on sensor-chip at day 1 and 10 (middle). Fluorescent images of liver chip at day 1 and
1086 10 of the transduced nuclear marker (bottom) **c.** Percentage of O2 level (black) and TEER
1087 impedance values (gray) on sensor Liver Chip during 10 days of culture. **d**. Average albumin
1088 production of Liver Chips at day of experiment start (day 7-10 of culture). **e**. Average urea
1089 production of Liver Chips at day of experiment start (day 7-10 of culture). **f.** Representative
1090 immunofluorescence images of the sensor Gut Chip (left) and Liver Chip (right) epithelium
1091 stained with DNA damage marker (H2AX) and nuclei (DAPI) for vehicle control and SNC80
1092 treated tissues after 7 days recovery. **g.** Quantitative analysis of proliferation and DNA damage
1093 stains on Gut and Liver Chips after 48h of treatment and 7-day recovery to 100μM SNC80 (2-3
1094 biological replicates/group/marker; each datapoint corresponds to an average of multiple fields
1095 of view). Statistical comparisons were performed using multiple unpaired t-tests for each marker
1096 with FDR correction. Data represent the mean±SD.

1097 **Figure S6. Metabolic measurements of Gut and Liver Chip systems treated with**
1098 **SNC80. a.** Monitoring the percentage change in barrier function of Gut (n=6 Chips/group) or **b**.
1099 Liver Chip (n=9 Chips/group) with time during treatment with 100μM SNC80 (0-48h) and

1100 recovery (48-120h) versus vehicle control Chip. **c**. Cytotoxicity measured for the Gut and **d.**
1101 Liver Chips during treatment and recovery. **e**. Graph depicting the amount of lactate measured
1102 in effluents of Gut and **f**. Liver Chips, relative to baseline levels (to day 7 for Gut and day 5 for
1103 Liver) for SNC80-treated (red) or vehicle control (black) Chips. **g**. Graph showing the glutamate
1104 measured in effluents of Gut or **h**. Liver Chips during SNC80 (red) or vehicle (black) treatment
1105 and post-recovery (day 7), relative to baseline levels. For each measurement, statistical
1106 comparisons were performed using multiple unpaired t-tests at each timepoint and FDR
1107 correction for multiple comparisons. Data represent the mean±SD.

1108 **Table S1. Clinical interpretation of ECG in SNC80 and vehicle treated hearts.**

1109

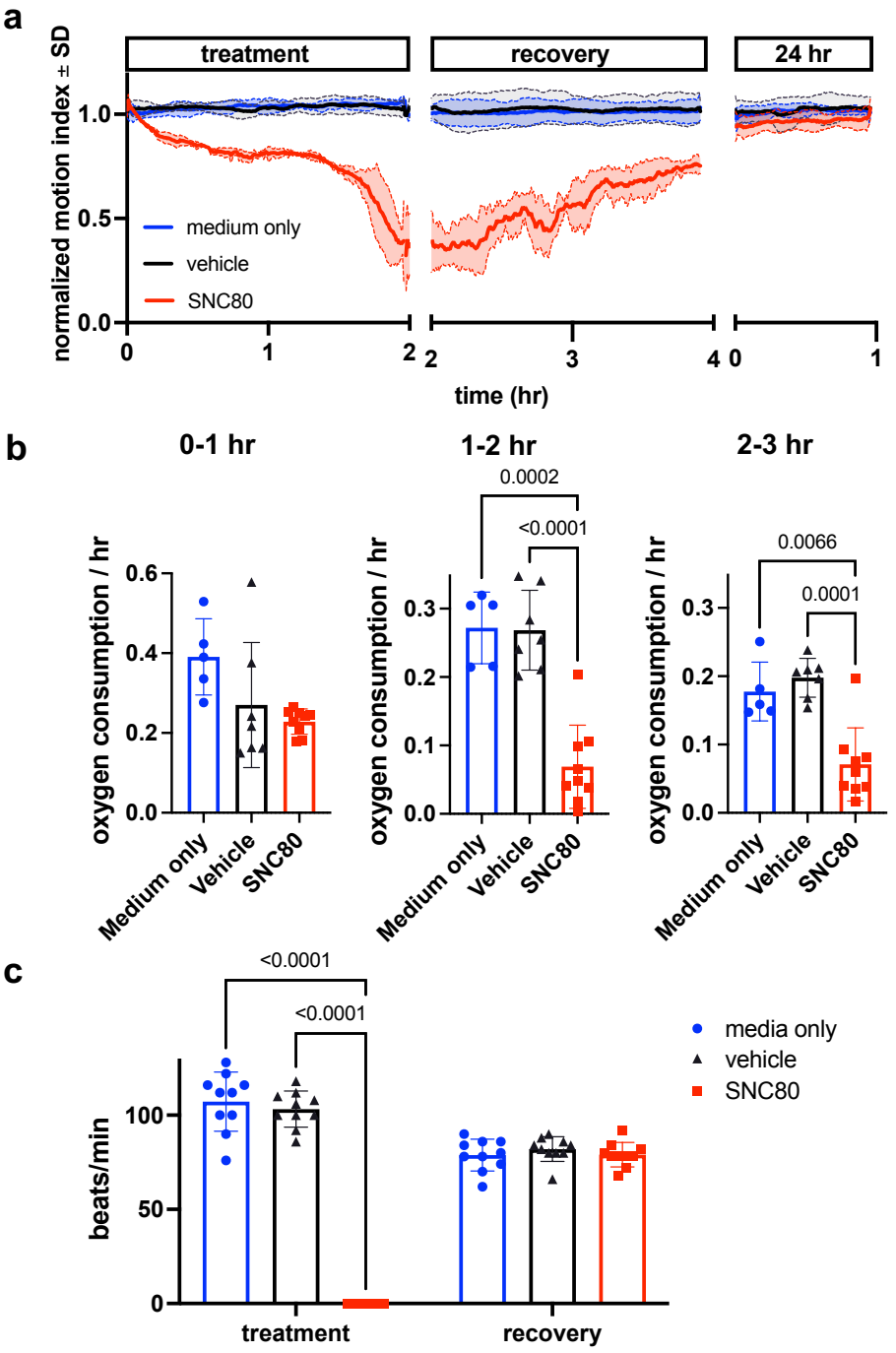

Figure 1

1110

1111

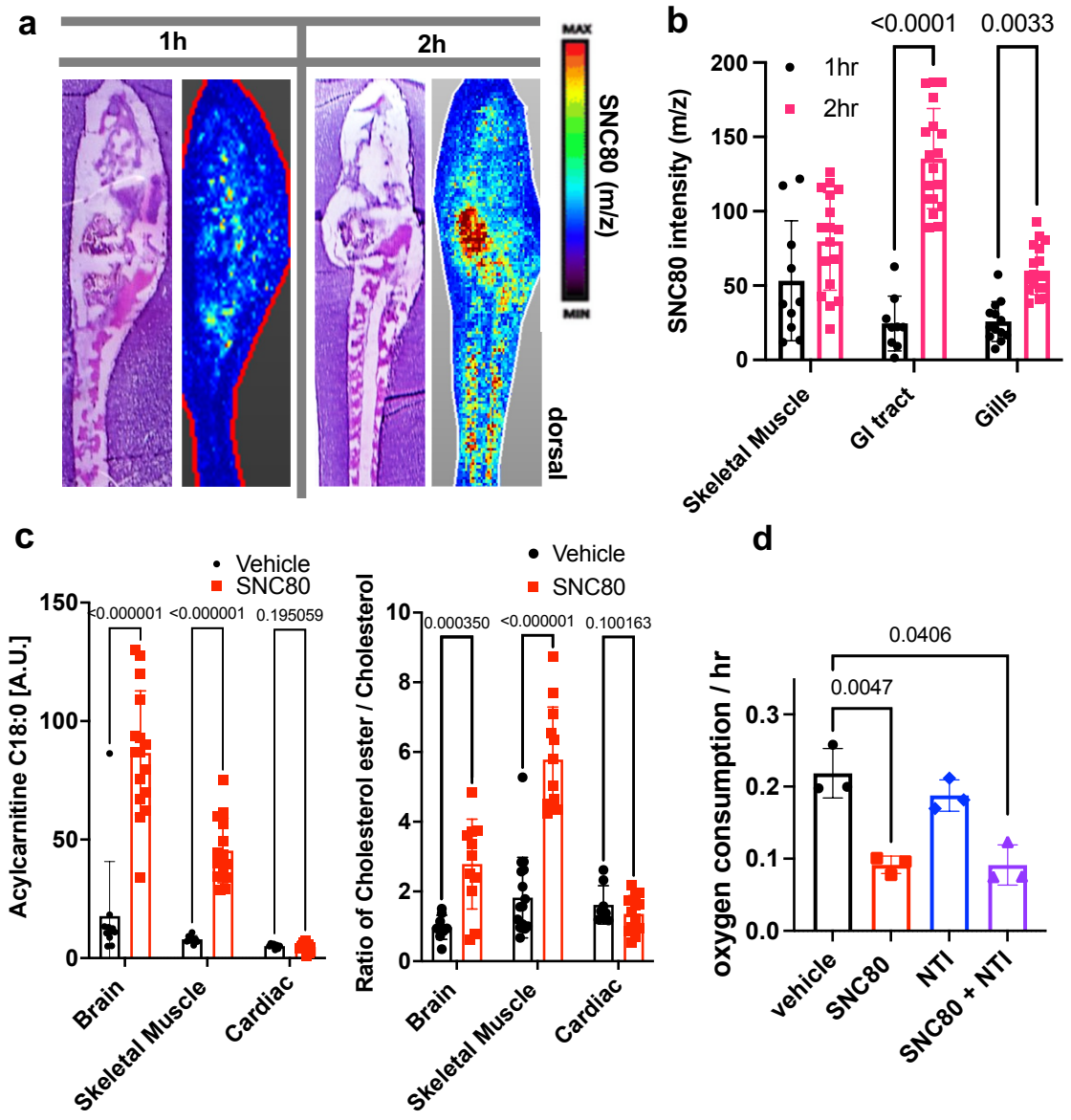

Figure 2

1112

1113

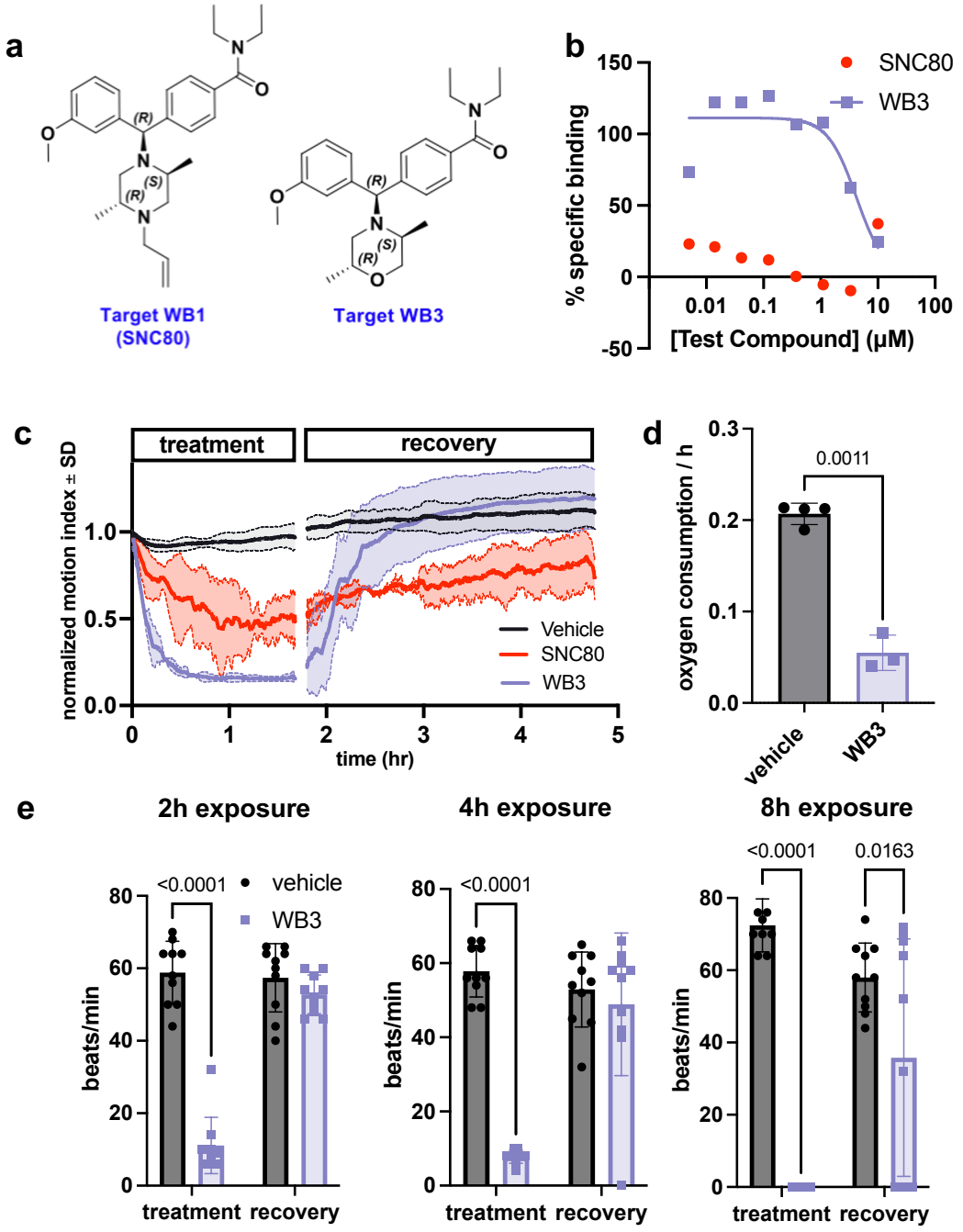

Figure 3

1114

1115

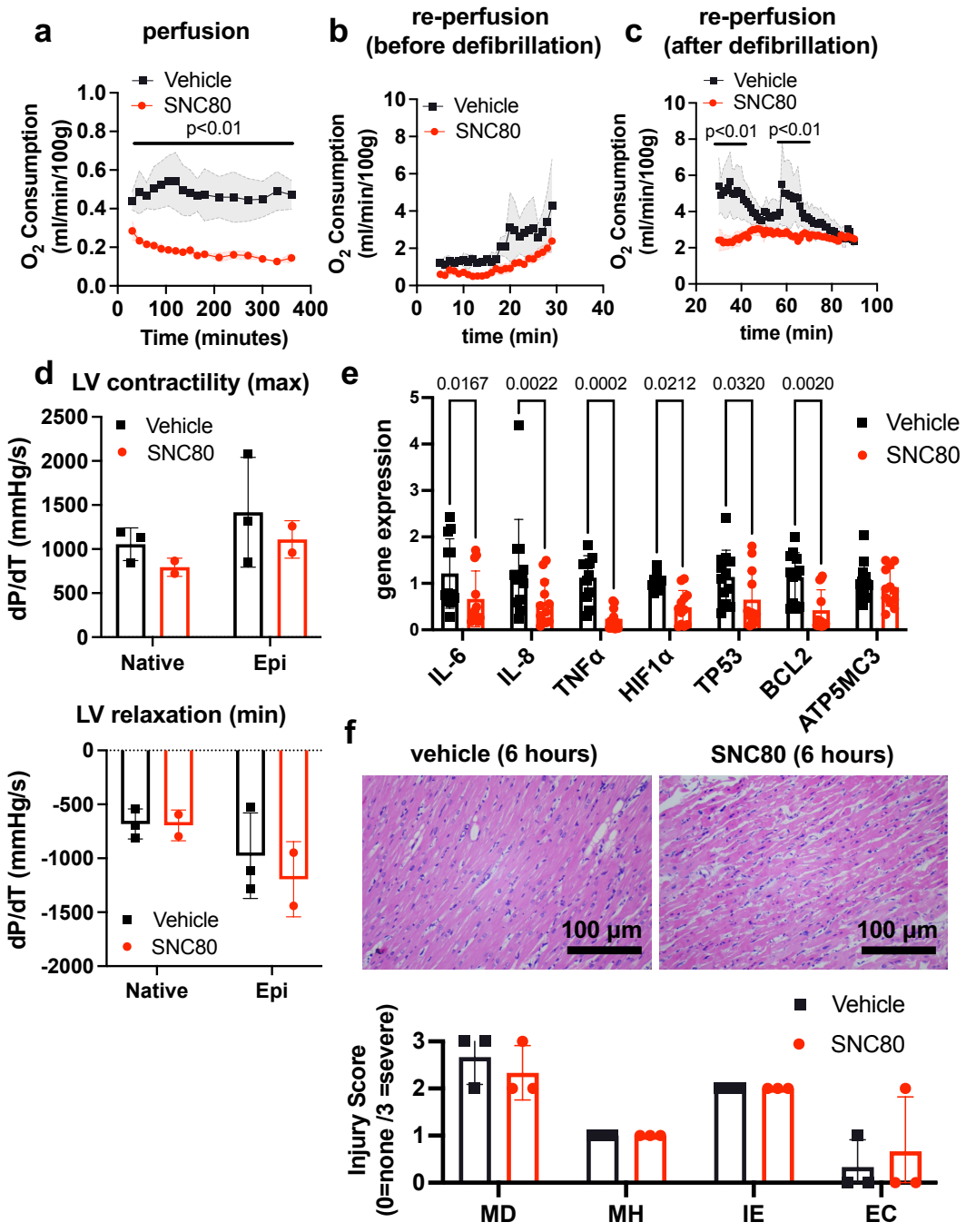

Figure 4

1116

1117

1118

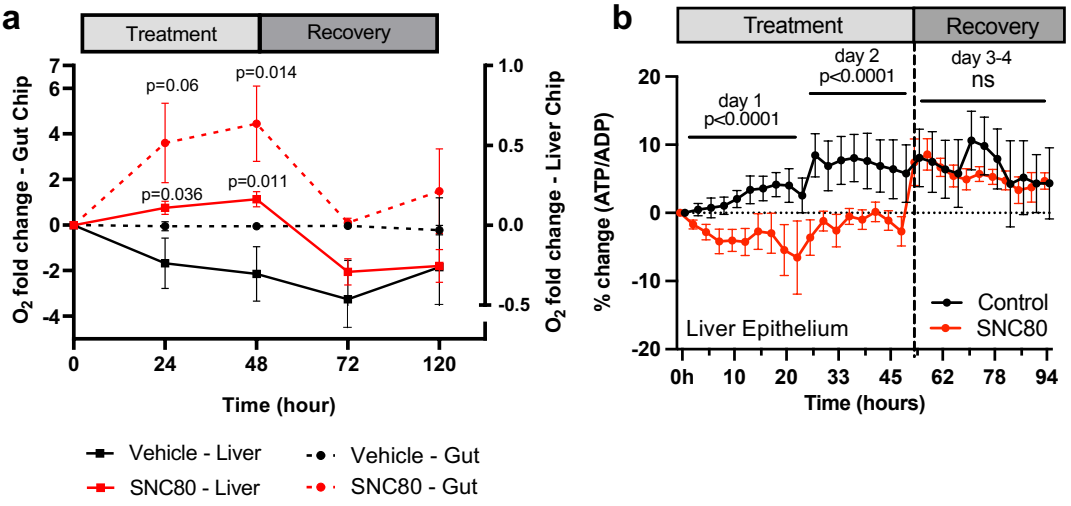

Figure 5

1119

1120

direct interaction	function	indirect interaction	function
CCBL1	• pyridoxal phosphate binding • cysteine-S-conjugate beta-lyase activity • L-glutamine aminotransferase activity • cellular modified amino acid metabolic process	ABCB1	• ABC-type bile acid transporter activity • regulation of fatty acid beta-oxidation • efflux transmembrane transporter activity
EAAT1	• L-glutamate transmembrane transporter activity	ACOX3	• fatty acid beta-oxidation using acyl-CoA oxidase • fatty acid binding
FUCA2	• alpha-L-fucosidase activity • glycoside catabolic process	CAMSAP2	• cytoplasmic microtubule organization • calmodulin binding
HM13	• peptidase activity • aspartic endopeptidase activity	COX6C	• mitochondrial electron transport, cytochrome c to oxygen • generation of precursor metabolites and energy
PTX3	• negative regulation of glycoprotein metabolic process • complement component C1q complex binding	ITGA7	• integrin-mediated signaling pathway • cell adhesion mediated by integrin
RPE65	• phosphatidylserine binding • retinoid metabolic process	NCX1	• calcium:sodium antiporter activity • calcium ion binding • regulation of the force of heart contraction
RPL27A	• structural constituent of ribosome cytoplasmic translation	ROBO1	• Roundabout signaling pathway • aorta development
RPL4	• structural constituent of ribosome cytoplasmic translation	RRP9	• RNA binding • rRNA processing
RPS25	• structural constituent of ribosome cytoplasmic translation		
TOMM40	• protein transmembrane transporter activity • protein targeting to mitochondrion • mitochondrial outer membrane translocase complex		
VMP1	• autophagosome membrane docking • plasma membrane phospholipid scrambling • lipoprotein transport		

Table 1

1121

1122

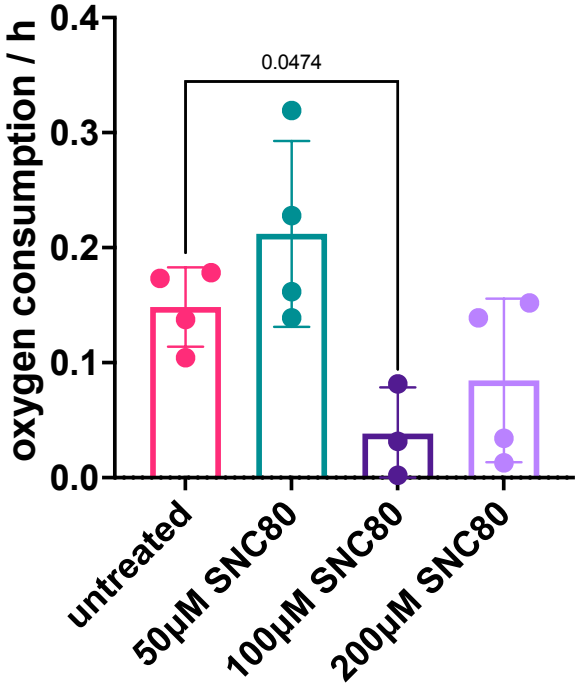

Supp. Figure S1

1123
1124

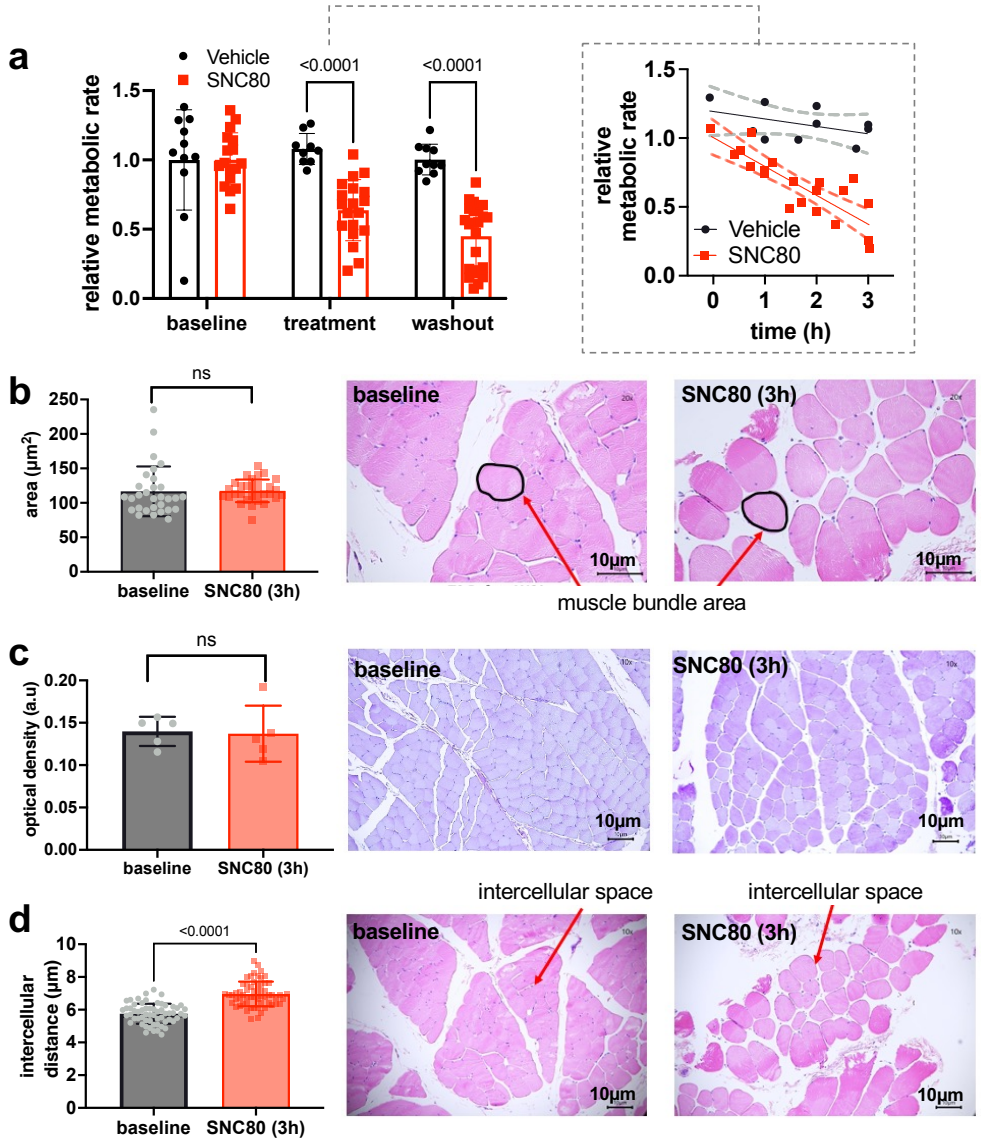

Supp. Figure S2

1125

1126

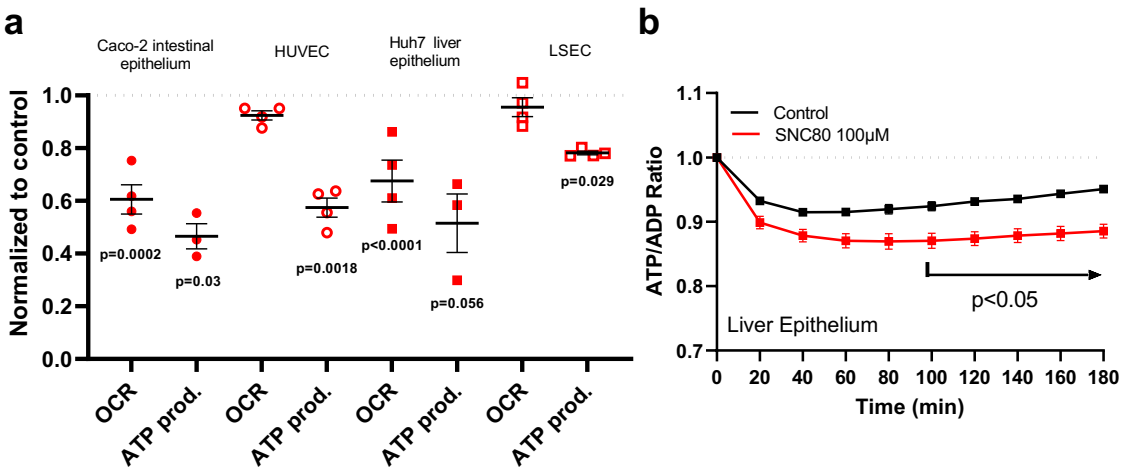

Supp. Figure S3

1127
1128
1129
1130

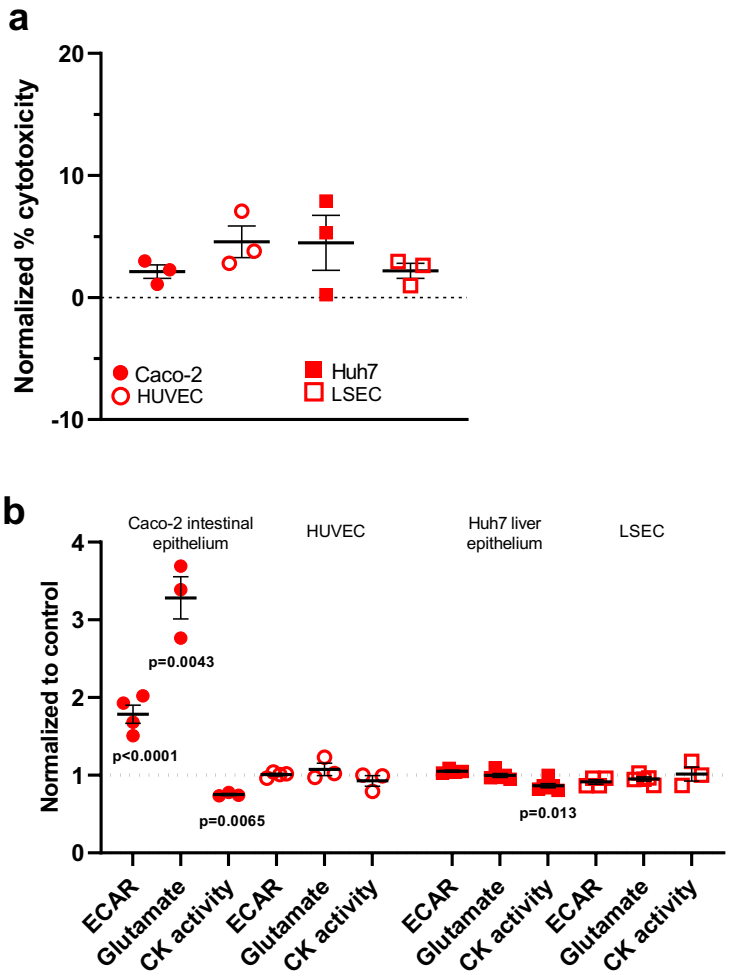

Supp. Figure S4

1131

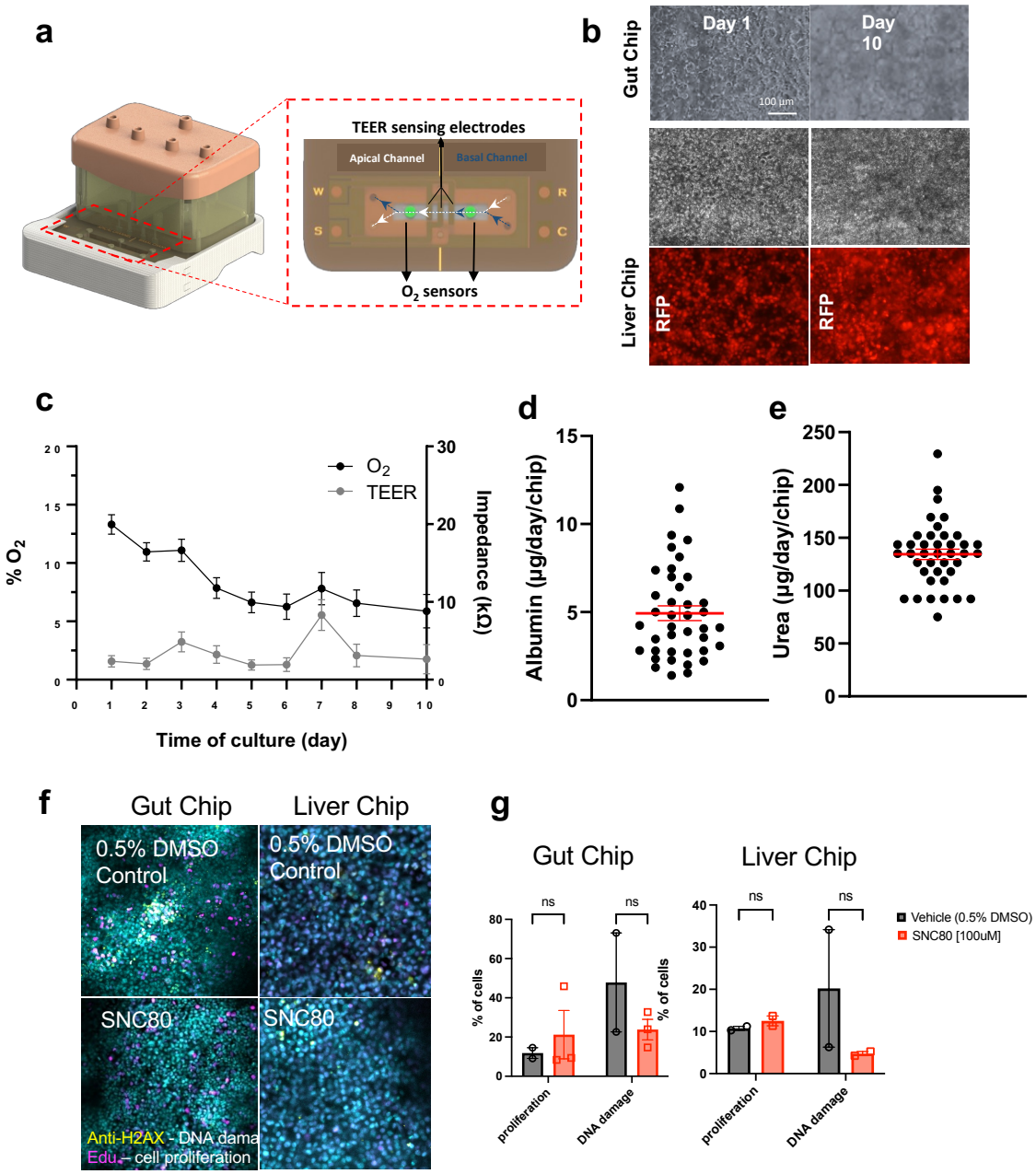

Supp. Figure S5

1132

1133
1134

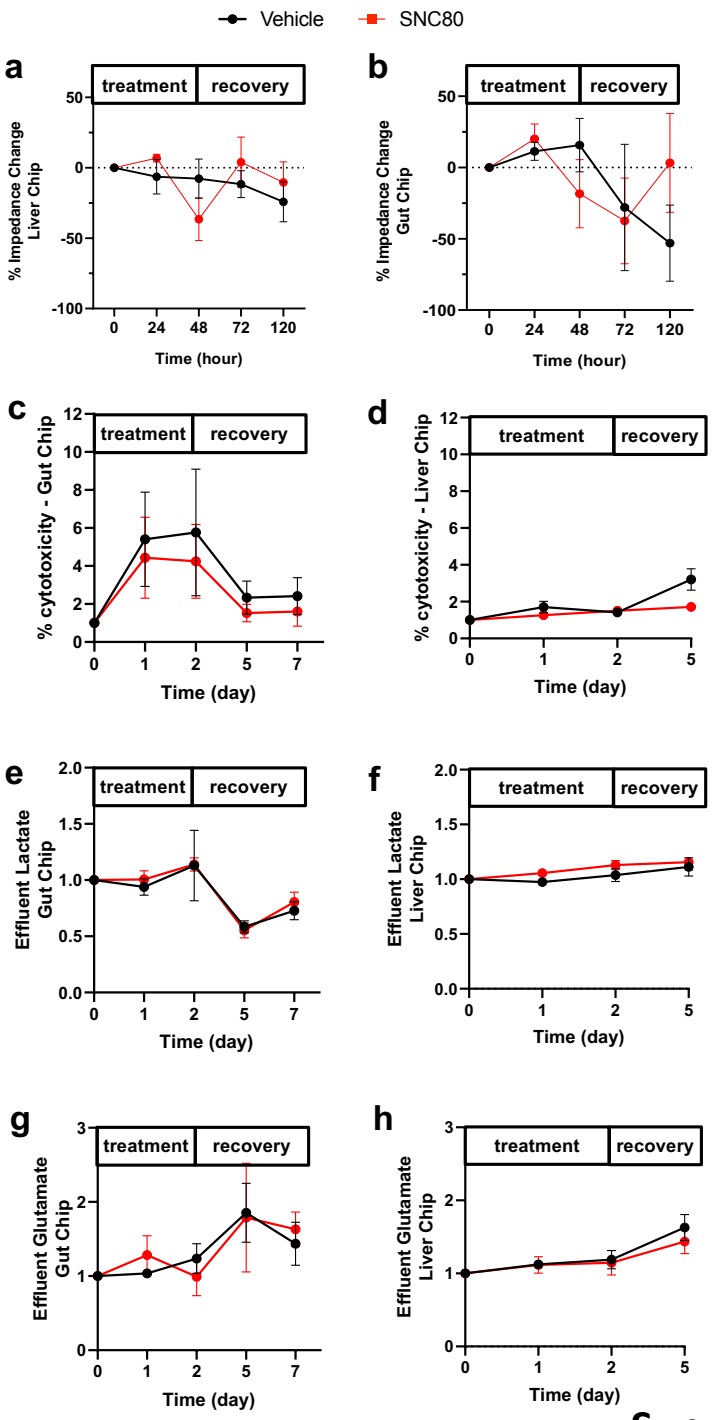

Supp. Figure S6

1135

1136

		Before recirculating					
		Pulse (bpm)	**Rate**	**Rhythm**	**P waves**	**QRS waves**	**T waves**
SNC80	P014	n/a	normocardic	irregular	no	no	n/a
	P015	n/a	tachycardic	irregular	no	no	n/a
	P019	n/a	n/a	n/a	n/a	n/a	n/a
	P023	12 bpm	bradycardic	irrregular	no	no	n/a
Vehicle	P016	n/a	tachycardic	irregular	no	no	n/a
	P020	n/a	tachycardic	irregular	no	no	n/a
	P024	n/a	tachycardia	irregular	no	no	n/a

		After defibrilation					
		Pulse (bpm)	**Rate**	**Rhythm**	**P waves**	**QRS waves**	**T waves**
SNC80	P014	132 bpm	tachycardic	regular	yes	yes	T wave elevation
	P015	96bpm	normocardic	irregular	yes	yes	Normal T waves
	P019	54 bpm	bradycardic	irregular	some	yes	Inconsistent T wave depression
	P023	96 bpm	normocardic	regular	no	no	Unable to assess (supraventricular tachycardia)
Vehicle	P016	144 bpm	tachycardic	regular	yes	yes	Slightly abnormal ST segment depression
	P020	132 bpm	tachycardic	regular	no	yes	T wave depression
	P024	138 bpm	tachycardic	regular	some	yes	T wave abnormal (P and T wave overlap)

Supp. Table S1

1137

1138

Supplemental Synthesis Description

<u>Step 1</u>: Synthesis of intermediate *N,N*-diethyl-4-formylbenzamide

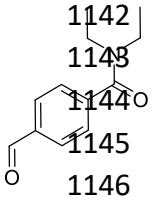

4-formylbenzoic acid (10 g, 66.61 mmol) and HATU (30.39 g, 79.93 mmol) were dissolved in DMF (500 mL) at 15 °C under N_2. The mixture was then warmed to 30 °C and stirred for 1 h. At this juncture, the mixture was cooled to 15 °C and DIEA (34.43 g, 266.43 mmol, 46.41 mL) and diethylamine (7.31 g, 99.91 mmol, 10.29 mL) were added dropwise together. The reaction was allowed to warm to rt and stirred for 12 h. The reaction mixture was diluted with H_2O (2000 mL), and then extracted with ethyl acetate (5000 mL x 3). The combined organic layers were washed with brine (1000 mL), dried over Na_2SO_4, filtered, and concentrated under reduced pressure to give a residue. The residue was purified by column chromatography (SiO_2, Petroleum ether/Ethyl acetate = 3/1 to 1/1) to give *N,N*-diethyl-4-formylbenzamide (57 g, 277.71 mmol, 83.38% yield) as a yellow solid. LC-MS m/z = 206.1 $[M+H]^+$.

<u>Step 2</u>: Synthesis of intermediate *N,N*-diethyl-4-[hydroxy(3-methoxyphenyl)methyl]benzamide

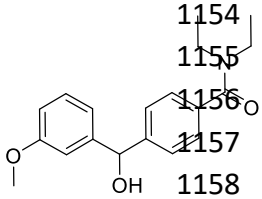

To a solution of *N,N*-diethyl-4-formylbenzamide (8 g, 38.98 mmol) in THF (320 mL) was dropwise added bromo-(3-methoxyphenyl)magnesium (1 M, 46.77 mL) at 0 °C under N_2. The reaction was stirred at 20 °C for 2 h, at which time it was diluted with H_2O (1000 mL), and then extracted with dichloromethane (500 mL x 3). The combined organic layers were washed with brine (300 mL), dried over Na_2SO_4, filtered, and concentrated under reduced pressure to give a residue. The residue was purified by column chromatography (SiO_2, Petroleum ether/Ethyl acetate = 3/1 to 1/1) to give *N,N*-diethyl-4-[hydroxy-(3-methoxyphenyl)methyl]benzamide (6 g, 19.15 mmol, 6.14% yield) as a white solid. LC-MS m/z = 314.1 $[M+H]^+$.

<u>Step 3:</u> Synthesis of intermediate 4-(chloro(3-methoxyphenyl)methyl)-*N,N*-diethylbenzamide

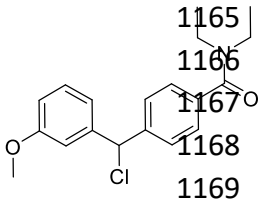

To a solution of *N,N*-diethyl-4-[hydroxy-(3-methoxyphenyl)methyl]benzamide (11.75 g, 37.49 mmol) in $CHCl_3$ (110 mL) was added dropwise HCl (12 M, 421.80 mL). The resulting mixture was stirred at 20 °C for 12 h, at which time it was diluted with H_2O (50 mL), and then extracted with dichloromethane (30 mL x 3). The combined organic layers were washed with brine (30 mL), dried over Na_2SO_4, filtered, and concentrated under reduced pressure to give 4-[chloro-(3-methoxyphenyl)methyl]-*N,N*-diethyl-benzamide (23 g, 69.31 mmol, 92.43% yield) as a yellow oil.

<u>Step 4:</u> Synthesis of WB3

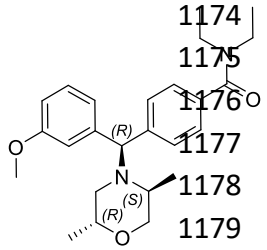

To a mixture of 4-[chloro-(3-methoxyphenyl)methyl]-*N,N*-diethyl-benzamide (23 g, 69.31 mmol) and (*2R,5S*)-2,5-dimethylmorpholine (15.97 g, 138.62 mmol) in ACN (230 mL) was added K_2CO_3 (19.16 g, 138.62 mmol). The resulting mixture was stirred at 80 °C for 4 days. The reaction mixture was filtered, and the mother liquor was directly concentrated. The residue was purified by column chromatography (SiO_2, Petroleum ether/Ethyl acetate = 5/1 to 2/1). The residue was further purified by preparative-HPLC (column: UniSil 10-120 C18 70x250mm; mobile phase: [water(FA)-ACN]; gradient:20%-50% B over 20 min) and the appropriate fractions were lyophilized. The residue was again further purified by preparative-HPLC (column: Phenomenex luna C18 (250*70mm,10 um); mobile phase: [water (FA)-ACN]; gradient:10%-50% B over 35 min) and the appropriate fractions were lyophilized to give WB3 (3.3 g, 8.03 mmol, 11.59% yield) as a white solid. LC-MS m/z = 296.1 $[M+H]^+$.

^{1}H NMR (400 MHz, $CDCl_3$) δ = 7.47 (d, J = 7.8 Hz, 2H), 7.34 - 7.27 (m, 3H), 6.88 (dd, *J* = 2.0, 8.3 Hz, 1H), 6.75 (d, *J* = 7.6 Hz, 1H), 6.72 - 6.67 (m, 1H), 5.32 (s, 1H), 3.81 (s, 3H), 3.76 - 3.66 (m, 2H), 3.64 - 3.45 (m, 2H), 3.44 - 3.24 (m, 3H), 2.61 (dd, *J* = 2.0, 11.6 Hz, 1H), 2.57 - 2.48 (m, 1H), 1.82 (dd, *J* = 9.5, 11.6 Hz, 1H), 1.24 (br d, *J* = 0.8 Hz, 3H), 1.12 (d, *J* = 6.1 Hz, 6H), 1.06 (d, *J* = 6.3 Hz, 3H).